UNIVERSITY OF CALIFORNIA, SAN DIEGO

Data-based acoustic and seismoacoustic sensing methods : differencing approaches for signal processing with minimum a priori information

A dissertation submitted in partial satisfaction of the
requirements for the degree
Doctor of Philosophy

in

Oceanography

by

Selda Yildiz

Committee in charge:

William A. Kuperman, Chair
Michael Buckingham
William Coles
Bruce Cornuelle
LeRoy M. Dorman
William Hodgkiss
Philippe Roux

2014

The dissertation of Selda Yildiz is approved, and it is acceptable in quality and form for publication on microfilm and electronically:

_____

_____

_____

_____

_____

_____

_____

Chair

University of California, San Diego

2014

TABLE OF CONTENTS

LIST OF FIGURES

ACKNOWLEDGEMENTS

First and foremost, I would like to sincerely thank William A. Kuperman, as my adviser and mentor, for guiding me throughout my PhD with his unique patience, kindness and enthusiasm. His intuition and understanding physical phenomena made the research more valuable; and the friendly and fun atmosphere he created was motivational and encouraging. I appreciate all of his contributions of time and ideas, which made this PhD experience a productive and pleasurable one.

In addition, I would like to thank Philippe Roux, who guided me through my research at ISTERRE in France and provided insightful comments which helped me improve this thesis. Additionally, I thank Michael Buckingham, and LeRoy M. Dorman for serving on my committee, for their valuable time, and advises, either for a conference practice talk, or a paper draft. I thank my committee members, William Hodgkiss, Bruce Cornelle, and William Coles for their time and providing insightful suggestions, which I highly appreciate. I want to thank my colleague and co-author Karim Sabra for his kind and patience guidance, and lively discussions which made this research more fun. Special thanks go to the MPL group, including Norissa Gastelum, Evelyn Doudera, and my colleagues Stephanie Fried, Caglar Yardim and Jit Sarkar, for having provided a friendly and fun work environment, and for all their help throughout the years. Thanks also go to my colleagues and co-authors: Christian Marandet and Sandrine Rakotonarivo for their helpful discussions.

Finally, I sincerely thank my parents, family and friends for their endless love

and support.

Chapter 2, in full, is a reprint of the material as it appears in the Geophysical Research Letters. Selda Yildiz, Karim Sabra, LeRoy M. Dorman, W. A. Kuperman, "Using hydroacoustic stations as water column seismometers", GRL, Vol. 40, 2573-2578, doi:10.1002/grl.50371, 2013.

Chapter 3, in full, is a reprint of the material as it appears in the Journal of the Acoustical Society of America. Yildiz S., P. Roux, S. T. Rakotonarivo, C. Marandet, W. A. Kuperman, "Target localization through a data-based sensitivity kernel: A perturbation approach applied to a multistatic configuration", The Journal of Acoustical Society of America, 135, 1800-1807 (2014), DOI:http://dx.doi.org/10.1121/1.4868362

The dissertation author was the primary researcher and author of this material.

VITA

2006	Bachelor of Science in Telecommunication Engineering, Istanbul Technical University
2008	Master of Science in Telecommunication Engineering, Istanbul Technical University
2014	Doctor of Philosophy in Oceanography Scripps Institution of Oceanography, University of California, San Diego

PUBLICATIONS

Journal papers

1. Yildiz S., P. Roux, S. T. Rakotonarivo, C. Marandet, W. A. Kuperman, "Target localization through a data-based sensitivity kernel: A perturbation approach applied to a multistatic configuration", *The Journal of Acoustical Society of America*, 135, 1800-1807 (2014), DOI:http://dx.doi.org/10.1121/1.4868362

2. Yildiz, S., K. Sabra, L. M. Dorman, and W. A. Kuperman, (2013), "Using hydroacoustic stations as water column seismometers", *Geophys. Res. Lett.*, Vol. 40, 2573-2578, doi:10.1002/grl.50371.

3. Dickey, T, Banner ML, Bhandari P, Boyd T, Carvalho L, Chang G, Chao Y, Czerski H, Darecki M, Dong C, Farmer D, Freeman S, Gemmrich J, Gernez P, Hall-Patch N, Holt B, Jiang S, Jones C, Kattawar G, LeBel D, Lenain L, Lewis M, Liu Y, Logan L, Manov D, Melville WK, Moline MA, Morison R, Nencioli F, Pegau WS, Reineman B, Robbins I, Rottgers R, Schultz H, Shen L, Shinki M, Slivkoff M, Sokolski M, Spada F, Statom N, Stramski D, Sutherland P, Twardowski M, Vagle S, Van Dommelen R, Voss K, Washburn L, Wei J, Wijesekera H, Wurl O, Yang D, Yildiz S, You Y, Yue DKP, Zaneveld R, Zappa CJ, (2012). "Introduction to special section on recent advances in the study of optical variability in the near-surface and upper ocean", *Journal of Geophysical Research-Oceans*, 117 10.1029/2012jc007964

4. Yildiz S., Altuncu Y., Yapar A., and Akduman I., "On the Scattering of Electromagnetic Waves by Periodic Rough Dielectric Surfaces: A BOA Solution", *IEEE Geoscience and Remote Sensing Letters*, Vol.46(9), 2599-2606, 2008

5. Mudanyali O., Yildiz S., Semerci O., Yapar A. and I. Akduman, "A Microwave Tomographic Approach for Non-Destructive Testing of Dielectric Coated Metallic Surfaces", *IEEE Geoscience and Remote Sensing Letters*, Vol.5(2), 180-184, 2008

Conference papers/talks

1. Yildiz S, L. M. Dorman, W. A. Kuperman, K. Sabra, P. Roux, D. Green, S. Fried, H. Schmidt, "Using hydrophones as vector sensors", *Acoustical Society of America (ASA)*, Providence, RI, USA, May 2014, *submitted*

2. Yildiz S., C. Marandet, S. Rakotonarivo, P. Roux, W. A. Kuperman, "Data-based sensitivity kernel in a highly reverberating cavity", *International Congress on Acoustics (ICA)*, Montreal, Canada, June 2013, presenter

3. Yildiz S., C. Marandet, S. Rakotonarivo, P. Roux, W. A. Kuperman, "Data-based sensitivity kernel localization", *Ambient Noise Imaging and Monitoring Workshop*, Cargese, Corsica, April 2013, poster presenter

4. Yildiz S., K. Sabra, W. A. Kuperman, L. M. Dorman, "Using hydroacoutic stations as water column seismometers", *Acoustical Society of America (ASA)*, Kansas City, USA, October 2012, presenter

5. Yildiz S., S. Fried, S. Walker, W. A. Kuperman, W.S.Hodgkiss, K. Sabra, "Cross correlation of noise beams between horizontal arrays", *European Conference on Underwater Acoustics (ECUA)*, Istanbul, Turkey, July 2010, presenter

6. Yildiz S., Y. Altuncu, O. Ozdemir , "Scattering of electromagnetic waves from periodic rough surfaces", *European Electromagnetics (EUROEM)*, Lausanne, Switzerland, July 2008, presenter

7. C. Tasdemir, O. Mudanyali, O. Semerci, S. Yildiz, and A. Yapar, "Non-destructive testing of dielectric layers with defects", *J. Phys.: Conf. Ser.*, 135 (2008) 012096 doi:10.1088/1742-6596/135/1/012096

8. Tasdemir C., O. Mudanyali, O. Semerci, S. Yildiz, and A. Yapar, "Non-destructive testing of defects on dielectric layers", *International Conf. on Inverse Problems in Engineering (ICIPE)*, Dourdan, France, June 2008

9. Yildiz S., Y. Altuncu, and F. Akleman, "An effective method for the scattering electromagnetic waves by periodic rough surfaces", *Progress in Electromagnetics (PIERS)*, Prague, Czech Republic, August 2007, presenter

10. Mudanyali O., S. Yildiz, and O. Semerci, "Reconstruction of perfectly conducting rough surfaces beyond a layered media", *Progress in Electromagnetics (PIERS)*, Beijng, China, March 2007, attendee

ABSTRACT OF THE DISSERTATION

Data-based acoustic and seismoacoustic sensing methods : differencing approaches for signal processing with minimum a priori information

by

Selda Yildiz

Doctor of Philosophy in Oceanography

University of California, San Diego, 2014

William A. Kuperman, Chair

The emphasis of this thesis is to use differencing approaches to develop data-based acoustic and seismoacoustic sensing methods (actively and passively) with minimal a priori information and modeling; such as extracting seismic information without using seismometers, performing an active localization in a complex medium without an accurate propagation model, and performing an active probing without active sources. The differencing methods are explored to extract information from ocean and laboratory data. Chapter two provides a simple vector sensor emulation analysis by differencing

the acoustic pressure fields. We test this concept by processing hydroacoustic data from Comprehensive Nuclear-Test-Ban Treaty Organization's (CTBTO) International Monitoring System (IMS) stations in the Indian Ocean, and comparing the obtained simulated seismograms to velocity records from a nearby island seismic station. We demonstrate the procedure with simple analyses of records of the Great Sumatra-Andaman Earthquake of 2004, and show that water column data can be used to emulate seismometer measurements. The demonstrated vector sensor emulation method provides a potential opportunity to employ ocean remote sensing methodologies in deep water regions, therefore providing supplemental seismic measurements. Chapter three demonstrates a target localization using a data-based sensitivity kernel (SK), a perturbation approach, without using a complicated model. Experimental confirmation of the method is obtained using a cylindrical tank and an aggregate of ping-pong balls as targets surrounded by acoustic sources and receivers in a multistatic configuration. The differencing approach is implemented as amplitude change between target-free and target-present fields. The experimental observations show that target localization is successful using only the direct path arrivals, and improves by including later arrivals from the tank wall and the bottom/surface reverberation. As a follow up study, ambient noise resident in the tank is analyzed with a motivation of active probing without active sources. Using the same laboratory-set up as in Chapter three, we show that it is possible to extract the acoustic response of the tank using only ambient noise recorded in the tank. The work presented here is a validation of early work in the ocean environment.

Chapter 1

Background

1.1 Introduction

Numerical models have become standard research tools in almost all disciplines of science including the field of ocean acoustics. However, lack of environmental information for inputs reduce the utility of these models. Nevertheless, complexity provides uniqueness in a data set that we would like to take advantage of. In particular the uniqueness of the data from either a radiating or scattering object is associated with its location. One approach to minimize the impact of the complexity of the environment between the object and the sensor(s) has been to employ differencing methods. Among these are differencing of field quantities that turn out to be related to using vector sensor data, sensitivity kernel methods and correlation processing.

The emphasis of this study is to explore differencing approaches to develop data-based seismic/acoustic sensing methods (actively and passively) using minimal a priori

information and modeling. The differencing approaches are implemented in frequency varying problems, from low frequency (<0.1 Hz) to high frequency ($\sim$10 kHz) regimes. For instance, Chapter two demonstrates how to extract low frequency (0.01-0.05Hz) seismic information without seismometers using a very simple analysis with a vector emulation method. The demonstrated method is based on differentiating the pressure fields between the hydrophones of International Monitoring System (IMS) to estimate the vector quantities analogous to what a seismometer would record. Due to their triplet design and spacing of within a fraction of wavelength of each other, it is possible to measure pressure gradient, which is proportional to particle velocity. Therefore, when employed with ocean remote sensing methodologies, the method proposed here might provide potential supplemental seismic measurements and more flexibility in station coverage in deep-water regions of the world.

Chapter three presents a data-based sensitivity kernel method, a perturbation approach, for a target localization in a highly reverberating medium without the use of a complex model. By measuring the amplitude difference without and with the target in a multi-static configuration in a cylindrical tank, a linear inverse problem is constructed whereby the solution is the target position. Furthermore, by using a set of multiple sources and receivers surrounding the target, the performance of the method is greatly increased. In the absence of a model, the medium is spatially sampled to build a data-based model that will be used to back-project the data. In a multistatic configuration, this spatial sampling can be performed by moving an active source that is surrounded by receivers in the medium, or by moving a passive target between a set of sources and

receivers, as is used in this study. These approaches do not require any prior information or estimation of the medium properties. The localization of one or a few targets is demonstrated using the direct-path only. We here take advantage of the complex data-set by including the later arrivals from the tank wall and the bottom/surface reverberation, which indeed enhances the localization.

Furthermore, using the same laboratory set-up in Chapter three, we explore the active probing without the use of active sources. Early work, such as in ocean acoustics, ultrasonics, geophysics, has shown that random noise data contains information about the environment, and this information can be extracted when the noise rob recordings are processed appropriately. Chapter four presents the use of ambient noise cross-correlations for an estimation of the local transfer function (i.e. Green‘s function) of the tank (without the target). This experimental study is a validation of early work done in the ocean environment, where no active measurements were done to validate the passive estimates of the Green's functions.

1.1.1 Hydroacoustics

The International Monitoring System (IMS) of the Comprehensive Test Ban Treaty Organization (CTBTO) deploys hydroacoustic station networks to detect sounds generated by explosions at or below the ocean surface [1]. The stations are originally deployed to explore the nuclear activity around the globe. The hydroacoustic network, consists of six hydrophone stations and five T-phase stations (see Figure 1.1), is a key component of the IMS, along with the other IMS networks, which include 50 primary

and 120 auxilary seismic stations, 60 infrasound, and 80 radionuclide stations.

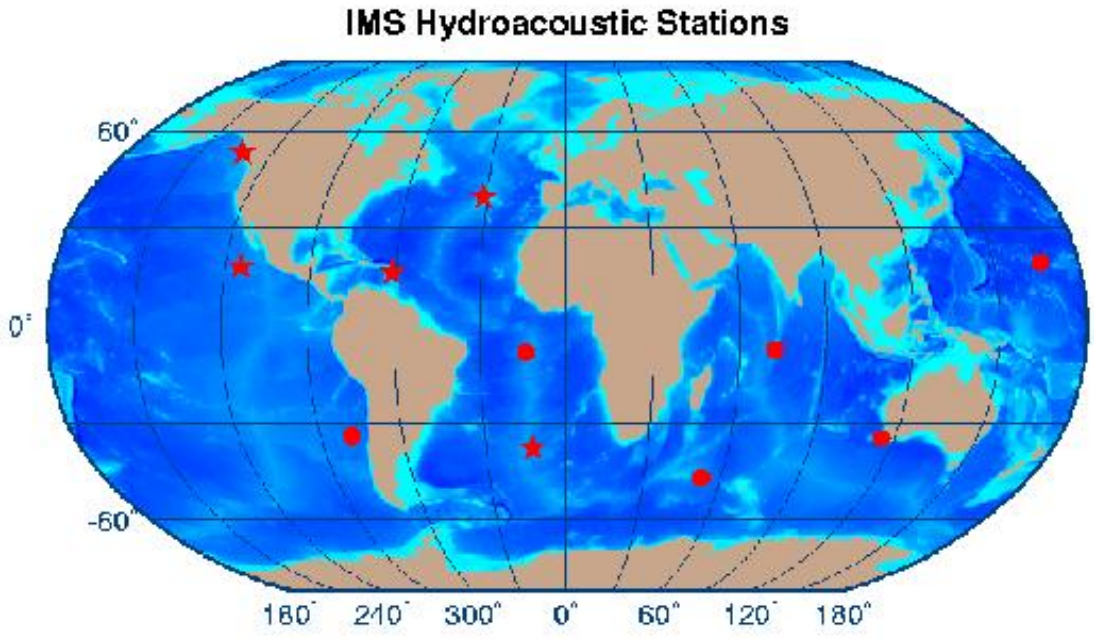

Figure 1.1: IMS Hydraouctic stations include five hydrophone stations (circles) and five T-phase stations (stars). Figure courtesy of the Acoustical Society of America, http://www.acoustics.org

Although the stations were originally deployed to monitor the nuclear activity around the world, the IMS network has been a valuable source for studying a broad range of scientific problems in the oceans: monitoring acoustics of nuclear explosions [2], estimating the rupture length of the December 2004 Great Sumatra earthquake [3], T-wave propagation [4], shipping noise [5], seismo-acoustics of ice sheets [6] and localization of Antarctic ice breaking events [7]. These studies, however, are at frequencies above 1 Hz and are predominantly of T-waves, which are generated by earthquakes along the plate margins [8].

IMS hydrophone networks

Figure 1.2 shows a typical hydrophone setup. Each hydroacoustic station has three hydrophones which are designed as triads with ~ 2 km spacing between them, and they continuously record at a sampling rate of 250 Hz. The hydrophones are moored to the seafloor and float at or near the depth of the deep sound channel, as underwater sounds within the Sound Fixing and Ranging channel (SOFAR) propagate over the long distances without a significant loss.

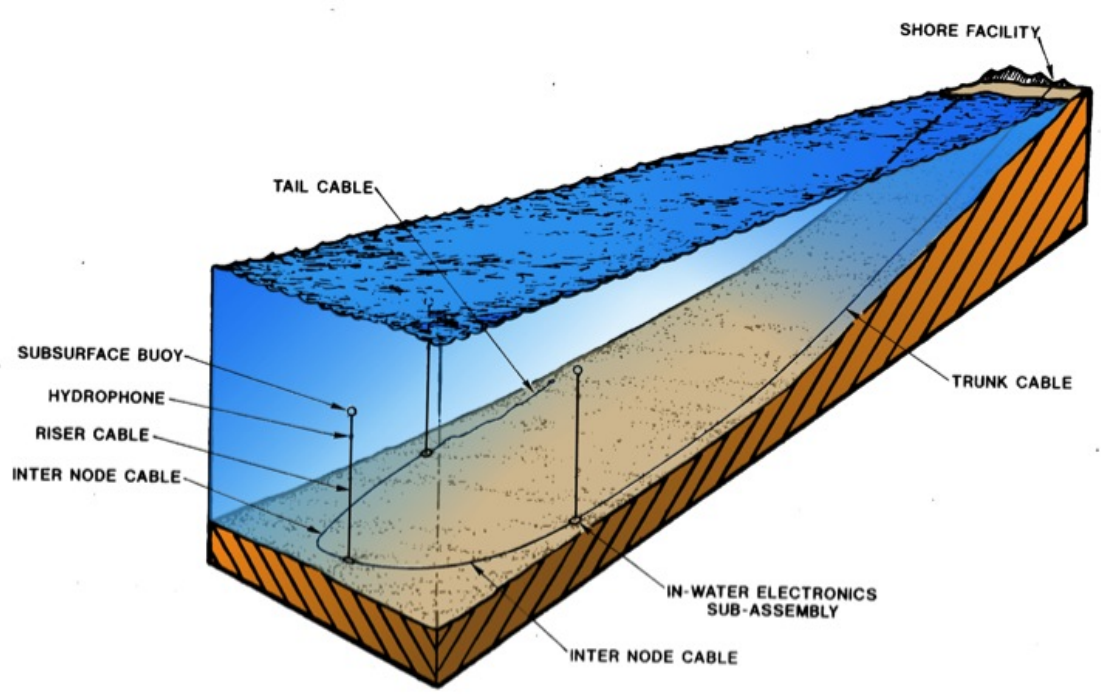

Figure 1.2: Setup of IMS hydrophone stations. Each station has three hydrophones, deployed at the depth of the deep sound channel, are designed in triplets with d=2 km sides. Figure courtesy of the Comprehensive Nuclear-Test-Ban Treaty Organization, www.ctbto.org.

The triplet design of the stations provides azimuthal directivity to locate acoustic and seismic events. For a given station, travel time delays between each hydrophone pair can be derived from the signal cross-correlations and inverted to determine the horizontal slowness, which then leads to back-azimuth to the source region [9, 10]. The slowness value obtained from the inversion, and the correlation coefficient (or closure value of the lag times), can be used to check the quality of the azimuthal estimations [11]. When multiple stations record the same event, localization using arrival times can benefit from a grid search or inversion routine which minimizes travel time residuals. [12].

Vector Sensor

In this section, background for vector sensor and processing is presented as a preparation for the vector sensor emulation method presented in Chapter two.

The concept of using acoustic vector sensors instead of traditional pressure sensors has been previously studied [13, 14, 15, 16]. As demand for smaller arrays performing better at a low signal-to-noise ratio (SNR) has risen, the interest in measuring the particle velocity along with the pressure has also risen [13]. Acoustic vector sensors have been used in directional sonobuoys deployed by the U.S.Navy community for the past-half century [17]. Although "DIFAR" (DIrectional low Frequency Analysis and Recording) sonobuoys have not often been used in scientific studies [for an exception, see Wilson, et al. (1985) [18]], recent studies in large baleen vocalization includes the use of acoustic vector sensors [19, 20, 21].

A vector sensor consists of two or three orthogonally aligned vector transducers, e.g., velocity , acceleration, and an omni-directional scalar pressure transducer, and standard array processing techniques for vector sensors are based on (a properly scaled) linear summation of those signals. Therefore, when a standard pressure sensor can utilize the directional information using propagation delays between sensors, a single vector sensor alone can extract directional information, up to two sources [14], directly from the structure of the velocity field. Further information on vector sensors and vector sensor beamforming can be found in [13, 22, 23].

In general, in ocean acoustics, directional properties of the ocean sound field is measured with a spatially distributed set of acoustic pressure sensors. An alternative approach can be obtained from the Taylor series expansion of the acoustic pressure field, $p(x,t)$, about a single measurement point in space, x_0 (e.g., [24]). Assuming that no acoustic source exists in the region about this point, then the acoustic pressure field can be expressed as [as in D'Spain et al [22]]:

$$p(x,t) = p(x_0,t) + \nabla p(x_0,t).\triangle x + \frac{1}{2}\triangle x^{\mathrm{T}} \left[\text{matrix of 2nd derivatives}\right] \triangle x + \ldots \quad (1.1)$$

where $\triangle x = x - x_0$. The measurement of acoustic pressure and its higher-order spatial derivatives at a single point in space is equivalent to the measurement of acoustic pressure in a volume about the measurement point. It provides the theoretical basis for array processing with measurements at a single point in space [24].

The acoustic wave equation is derived from the following forms of the conservation of mass and momentum,

$$\frac{\partial p(x,t)}{\partial t} + K_s(x)\nabla \cdot v(x,t) = 0, \tag{1.2}$$

$$\rho_0(x)\frac{\partial v(x,t)}{\partial t} + \nabla p(x,t) = 0, \tag{1.3}$$

where $\rho_0(x)$ is the ambient density and $K_s(x)$ is the adiabatic incompressibility. The acoustic variables $p(x,t)$ and $v(x,t)$ are the pressure and particle velocicty, respectively. These two equations describe all the physics needed for understanding the sound propagation and they hold for regions where no acoustic sources exist. Eq. 1.3 shows that acoustic particle velocity at a given frequency is proportional to the first-order spatial gradient of pressure. One implication of this equtaion is that if the acoustic pressure field is measured/known everywhere within a given region in space, the corresponding acoustic particle velocity field can be derived everywhere within the same region [22].

In the study presented in Chapter two, the velocity sensor is taken to be located at the center of the three hydrophones and a Taylor series expansion of the acoustic pressure field is used between each couple of hydrophones j and k as

$$P_j = P_k + \frac{\partial P}{\partial x}(x_j - x_k) + \frac{\partial P}{\partial y}(y_j - y_k) \tag{1.4}$$

Solution of pressure gradient in x and y includes a set of six equations where $j = 1,2,3,$

$k = 1, 2, 3$, and $j \neq k$. The particle velocity components v_x and v_y can be obtained using the relationship between the gradient of acoustic pressure and the particle velocity as

$$v = -\frac{i}{\omega\rho}\nabla P \tag{1.5}$$

where ω is angular frequency and ρ is the local ambient density of the fluid medium. The vertical particle velocity component v_z is measured using depth differences of hydrophones in each station. To get the radial and transverse components of the velocity relative to aspecified direction, v_x and v_y are rotated based on azimuthal angle.

1.1.2 Target localization

In underwater acoustics, sonar networks have been explored for target detection and localization; and monostatic, bistatic, and multistatic approaches have been compared in terms of their performance [25, 26, 27, 28]. Multistatic sonfiguration have received attention as it enhances the performance of target detection and localization by increasing the survey coverage rate and providing a range of scattering angles for a given target thus allowing to exploit the spatial diversity of the target's acoustic response [29]. Generally, the source signal for monostatic sonar needs to be loud enough to make the backscattered echo emerge from the ambient noise, as the back scattering of a target is weak. Therefore, as the echo amplitude is higher than in back-scattering. detecting a target by exploiting its forward scattering is of interest. The classic difficulty in such case is that the scattered field must be extracted from the direct-arriving field,

i.e., often referred to as “looking into the sunlight problem” [30, 31]. The difficulty of extracting forward scattering from the usually much more intense and sometimes fluctuating, direct-arrivals has been addressed in an acoustic barrier problem [32, 33]. A time-reversal method has been suggested to account for the reverberation and scattering from the boundaries that often limit sonar performance in a shallow-water configuration. A time-reversal detection in forward propagation might be robust to environmental fluctuations (such as surface waves). However, it does not indicate the target location. Additionally, another study used time reversal for the detection and localization of a target on the seafloor in the presence of bottom scattering using laboratory-scale data [34].

Recently, some studies on target detection and localization have been published using a beamforming technique on a receiver array placed in front of some acoustic sources [35]. The presence of the target was detected through the shadowing effects observed on a set of beamformed beams. Depending on the number of perturbed eigenbeams, the target localization was achieved using a forward or inverse problem [35, 36]. The practical disadvantage of this approach is the requirement for two well-sampled source and receiver arrays that provide a two-dimensional localization that is limited to the plane defined by the arrays.

1.1.3 Sensitivity kernel

Sensitivity kernel (SK) describes the relationship between the changes in the acoustic field propagating in a medium and a local perturbation [37]. In practice, SKs

are calculated as the change in the field associated with a local heterogeneity between a source-receiver pair. The position of a perturbation and its physical nature influences the acoustic field at the receiver. In underwater acoustics, SKs has been used in travel time tomography [38], for a perturbation in sound speed [39], density [36] , or for surface scattering in a waveguide [40]. As well as from its straightforward use in the forward problem, the SK formulation can be used to invert for environment fluctuations between a source−receiver pair [41, 42, 39]. Finally, a recent study has shown that the experimental measurement of the SK between a source and a receiver matches favorably to numerical calculations using both the direct and reflected path at the ultrasonic scale [43].

Volume Perturbation

In this section, a theoretical formulation of the sensitivity kernel for a volume perturbation is presented, i.e. sound-speed.

The Green's function $G(r, r_s)$ of an ocean acoustic waveguide, for the acoustic field of a harmonic point of unit strength source, satisfies the following wave equation:

$$\nabla^2 G(r, r_s) + \frac{\omega^2}{c^2} G(r, r_s) = -\delta(r - r_s), \tag{1.6}$$

If the volume perturbation is a sound speed change $\Delta c(r')$, the wave equation for

the perturbed field is

$$\nabla^2 G(r,r_s) + \frac{\omega^2}{[c+\Delta c(r')]^2} G(r,r_s) = -\delta(r-r_s), \tag{1.7}$$

which, to lowest order is

$$\nabla^2 G(r,r_s) + k^2 G(r,r_s) = -\delta(r-r_s) + \frac{2\omega^2 \Delta c(r')}{c^3} G(r',r_s). \tag{1.8}$$

The Born approximation then gives

$$\begin{aligned} &G(r,r_s) - G_0(r,r_s) \equiv \\ &\Delta G = -2\omega^2 \int_V G_0(r,r') G_0(r',r_s) \frac{\Delta c(r')}{c(r')^3} dV(r'), \end{aligned} \tag{1.9}$$

which translates to the sensitivity of the Green's function to a sound speed perturbation,

$$\frac{\partial \Delta G(r|r')}{\partial \Delta c(r')} = -2\omega^2 G(r|r') G(r'|r_s) \frac{1}{c(r')^3}, \tag{1.10}$$

where we have made an obvious change in notation.

Since the pressure field from a broadband source at receiver r_r (see Figure 1.3) is

$$p_r(t) = \frac{1}{2\pi} \int_{-\infty}^{\infty} G(r_r|r_s;\omega;c) P_s(\omega) e^{i\omega t}\, d\omega, \tag{1.11}$$

and the perturbed pressure is of the same Fourier form, we have

$$\frac{\partial p_r(t)}{\partial c(r')} = \frac{1}{2\pi}\int_{-\infty}^{\infty}\left(-2\omega^2 G(r_r|r')G(r'|r_s)\frac{P_s(\omega)}{c(r')^3}\right)e^{i\omega t}\,d\omega. \tag{1.12}$$

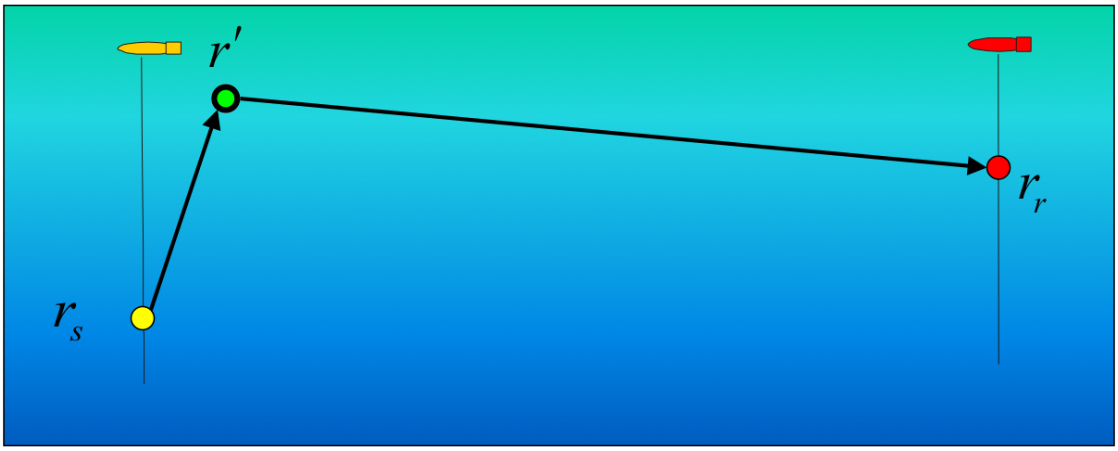

Figure 1.3: Schematic diagram of the source in r_s, the receiver in r_r, and the local change in r'. The change in the measured impulse response due to a change at a point r' in the medium is simply a function of the propagation to that point from the source, and then on to the receiver from the point.

Inversion using the sensitivity kernel

We rewrite Eq. 1.12 as

$$\Delta p = \frac{\partial p}{\partial c}\Delta c, \tag{1.13}$$

where the partial derivative is given by Eq. 1.12 and Δp and Δc are each column vectors of dimension M, the number of spatial positions of the perturbation. Here the sensitivity kernel is a matrix whose N_r rows, each corresponding to a receiver, are of length M. Hence, each row times the column vector of sound speed perturbations is the pressure

perturbation at the $r-$th receiver. In element notation, Eq. 1.13 can be written as

$$\Delta p_{n_r} = \frac{\partial p_{n_r}}{\partial c_m} \Delta c_m. \tag{1.14}$$

Now, all the above refers to one source and multiple receivers. We can expand the to many sources by increasing the length of pressure perturbation vector to $N_r \times N_s \equiv N$ and correspondingly, increasing the numbers of rows of the sensitivity kerne matrix to N. Writing the *lhs* of Eq. 1.13 as a perturbation data vector (model - data) of length N, we have

$$d = H\Delta c \tag{1.15}$$

or, in element notation,

$$d_n = H_{nm}\Delta c_m. \tag{1.16}$$

Even though we have many more rows than column(less measurements than perturbations), we can "invert" Eq. 1.16 to get an estimate

$$\widehat{\Delta c} = H^{+} d \tag{1.17}$$

where $+$ indicates the pseudoinverse.

1.1.4 Noise as the signal

Early work has shown that random noise data contains information about the environment, and this information can be extracted when the noise recordings are processed appropriately. Both incoherent and coherent processing of ambient noise can be successful and provide a foundation for passive sensing and imaging without active transmitters. For instance, ocean noise is the acoustic equivalent of diffuse acoustic daylight, and incoherent processing of ambient noise can be used for underwater imaging [44]. Although the acoustic field due to random noise sources is often considered incoherent, coherent processing of noise recordings is possible, as there is some coherence between the sensors receiving signals from same individual noise source. In fact, the impulse response between two sensors can be extracted by cross-correlating the noise recordings at these sensors [45, 46]. With laboratory measurements of acoustic thermal fluctuations, Weaver and Lobkis confirmed that the cross-correlation of the ambient noise at two sensors can provide an estimate of the time domain Green's function (TDGF) as if one sensor was a source, and the other one was receiver. The arrival times and strengths of the cross correlation peaks emerge from the accumulated contributions from noise sources whose propagation path pass through both receivers. These paths are the same as if the noise occurs at one location and is recorded at the second, or if noise propagates through both locations, the ray paths are a function of the environment, not the source signal.

This approach has been expanded to ultrasonics [45, 47, 48], underwater acous-

tics [49, 50, 51], structural-health monitoring [52, 53], and geoacoustic imaging [54, 55, 56]. In addition, using surface velocity and intensity fields, a similar method in helioseismology is developed to image the propagation of solar waves through sunspots [57, 58, 59, 60].

1.2 Work presented

This thesis aims to develop data-based acoustic and seismoacoustic sensing methods by employing differencing approaches. One of the main motivation here is to keep signal processing/analysis simple by using minimum a priori information and focusing on data-based analysis rather than developing complex numerical models. The main focus in Chapter two, three, and four, respectively is to (1) extract seismic information without using seismometers with a simple pressure gradient analysis, (2) to perform an active localization without a complex propagation model in a highly reverberating medium (3) to perform an active probing without active sources, where the differencing approach is implemented as (1) pressure gradient to get the vector quantities analogous to seismic data, (2) change in field amplitudes between with and without the target cases, (3) cross-correlations as a measure of the difference of ambient noise recorded at the receivers.

In Chapter two, we show that it is possible to extract seismic information using hydroacoustic data, without using seismometers. Getting seismic data from the deep oceans usually involves ocean-bottom seismometers, but hydrophone arrays may pro-

vide a practical alternative means of obtaining vector data. The hydroacoustic stations of the International Monitoring System (IMS) have been used to study icebergs and T-wave propagation among others. These studies, however, are at frequencies above 1 Hz and int his study, we use data from these stations in the very low frequency regime $f = 0.01 - 0.05$ Hz, to demonstrate that these stations can also be used as water column seismometers. These stations consist of three hydrophones at about the depth of the deep sound channel in a horizontal triangle array with 2 km sides. Measuring the pressure gradient between two closely separated (with respect to wavelength) points is equivalent to a velocity measurement. Thus within this low frequency band, by differencing the acoustic pressure, we obtain vector quantities analogous to what a seismometer would record. Comparing processed hydrophone station records of the 2004 Great Sumatra-Andaman Earthquake with broadband seismograms from a nearby island station, we find that the differenced hydrophones are indeed a practical surrogate for seismometers. Consistent with the physics, transverse Love waves in the water column do not couple, whereas P waves and Rayleigh waves with radial and vertical motion do couple at the water-sediment interface. A slowness analysis using only the pressure recordings at the three hydrophones has shown that it is possible to determine the direction of the source location at a single station.

The main focus of the study presented in Chapter three is to use a multistatic configuration and a data-based method to localize a target in three dimensions without the use of an accurate propagation model. The method is based on a finite-frequency perturbation approach, through the measurement of a data-based sensitivity kernel. The

idea is to focus on the amplitude change in the direct-path signals between without and with the perturbation (the target) in the medium. In the absence of a model, the medium is spatially sampled to build a data-based model that will be used to back-project the data. In a multistatic configuration, this spatial sampling can be performed by a moving active source that is surrounded by receivers in the medium, or by moving a passive target between a set of sources and receivers, as is used in this study. These approaches do not require any prior information or estimation of the medium properties. Experimental confirmation of the method is obtained using a cylindrical tank and an aggregate of ping-pong balls as targets surrounded by acoustic sources and receivers in a multistatic configuration. The spatial structure of the sensitivity kernel is constructed from field data for the target at a sparse set of positions, and compared with the expected theoretical structure. The localization of one or a few targets is demonstrated using the direct-path only. The experimental observations also show that the method benefits from including later arrivals from the tank wall and the bottom/surface reverberation, which indeed improves the localization results. Furthermore, by using a set of multiple sources and receivers surrounding the target, the performance of the method is greatly increased.

Finally, Chapter four examines active probing using only ambient noise, without active sources. The data analysis shows that extracting the transfer function from active sources is possible using only ambient noise resident in the medium. The efficacy of the analysis is confirmed in an experiment inside a fish tank, as in Chapter two, using several frequency bands ($f = 0.5 - 1.5$ kHz, $f = 1 - 3$ kHz, $f = 2 - 4$ kHz). By comparing the active and passive measurements, the noise correlation results shown within this

laboratory set-up provide a validation of the early work that has been done in the ocean environment.

Chapter 2

Using hydroacoustic stations as water column seismometers

Getting seismic data from the deep oceans usually involves ocean-bottom seismometers, but hydrophone arrays may provide a practical alternative means of obtaining vector data. We here explore this possibility using hydrophone stations of the International Monitoring System (IMS), which have been used to study icebergs and T-wave propagation among others. These stations consist of three hydrophones at about the depth of the deep sound channel in a horizontal triangle array with 2 km sides. We use data from these stations in the very low frequency regime (0.01 - 0.05 Hz band), to demonstrate that these stations can also be used as water column seismometers. By differencing the acoustic pressure, we obtain vector quantities analogous to what a seismometer would record. Comparing processed hydrophone station records of the 2004 Great Sumatra-Andaman Earthquake with broadband seismograms from a nearby is-

land station, we find that the differenced hydrophones are indeed a practical surrogate for seismometers.

2.1 Introduction

Earthquake seismology suffers from an extreme continental bias. While broadband seismometers on islands fill some of the holes in coverage, vast tracts of the deep ocean remain uninstrumented. Getting seismic data from the deep ocean typically requires ocean-bottom seismometers, with all the deployment, coupling, and data recovery problems inherent in such instruments. Hydrophones, on the contrary, are intrinsically simpler, but provide only the scalar pressure rather than the vector quantity desired. However, it should be possible to simulate seismic data by taking the appropriate spatial derivative of data from tripartite hydrophone arrays in the ocean. Those derivatives could simply be approximated by taking first differences. Pressure sensors, therefore, spaced within a small fraction of a wavelength of each other can be used to measure particle displacement, velocity or acceleration analogous to measurements from a seismometer.

Recent trends in ocean acoustics include ocean remote sensing methodologies (e.g., [61]) with data sampling rates and navigation accuracy substantially higher than seismic requirements. The method demonstrated in this paper, therefore, provides a potential opportunity to employ this technology in deep water regions for supplemental seismic measurements and also giving more flexibility in station coverage.

The IMS is a valuable source for studying a broad range of scientific problems in the oceans: monitoring acoustics of nuclear explosions [2], estimating the rupture length of the December 2004 Great Sumatra earthquake

[3], T-wave propagation [4], shipping noise [5], seismo-acoustics of ice sheets [6] and localization of Antarctic ice breaking events [7]. These studies, however, are at frequencies above 1 Hz and are predominantly of T-waves, which are generated by earthquakes along the plate margins [8].

In this paper, we show how low-frequency vector seismic data can be extracted from hydrophone array data by computing pressure gradients. From the appropriate pressure gradient records we can simulate vertical, radial, and transverse velocity traces, although the transverse traces will not show Love waves since Love waves do not couple significantly into the water column as the viscous slip layer in the water column is only on the order of 10m [62]. We test this concept by processing hydroacoustic data from Comprehensive Nuclear-Test-Ban Treaty Organization's (CTBTO) IMS stations in the Indian Ocean, and comparing the obtained simulated seismograms to velocity records from a nearby island seismic station. We demonstrate the procedure with simple analyses of records of the Great Sumatra-Andaman Earthquake of 2004 and show that water column data can be used to emulate seismometer measurements.

2.2 Vector Sensor Emulation from the IMS Hydrophone Triad

The IMS hydroacoustic stations are designed horizontally in triplets with sides of approximately 2 km length; each station is deployed at or near the depth of the deep sound channel. To be able to use the hydroacoustic stations at this low frequency regime (f= 0.01 - 0.05 Hz), hydrophone data are transformed to vector velocity using pressure gradients. Measuring the pressure gradient between two closely separated (with respect to wavelength) points is equivalent to a velocity measurement [63]. Referring to Figure 2.1, we take this velocity sensor to be located at the center of the three hydrophones and use a Taylor series expansion of the acoustic pressure field between each couple of hydrophones j and k as

$$P_j = P_k + \frac{\partial P}{\partial x}(x_j - x_k) + \frac{\partial P}{\partial y}(y_j - y_k) \tag{2.1}$$

Solution of pressure gradient in x and y includes a set of six equations where $j = 1,2,3$, $k = 1,2,3$, and $j \neq k$. The particle velocity components v_x and v_y can be obtained using the relationship between the gradient of acoustic pressure and the particle velocity as

$$v = -\frac{i}{\omega\rho}\nabla P \tag{2.2}$$

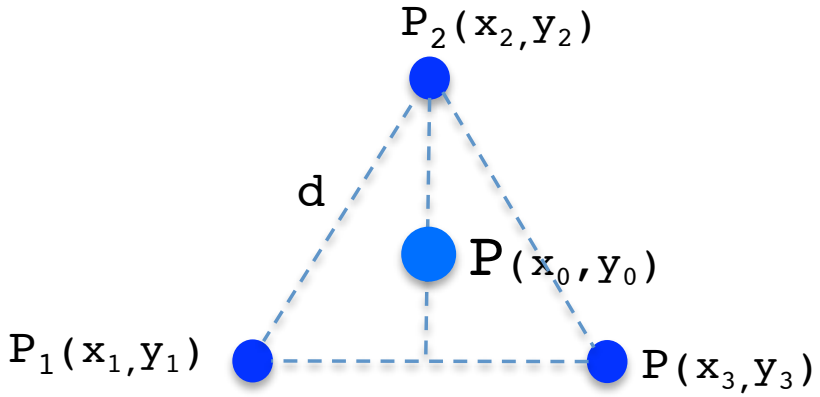

Figure 2.1: Pressure gradient representation for a hydroacoustic triad station with d=2 km sides. The three hydrophone configuration allows one to compute pressure and the three velocity components at the affective center of the hydroacoustic station at the very low frequency regime (f<0.1 Hz)

where ω is angular frequency and ρ is the local ambient density of the fluid medium. The vertical particle velocity component v_z is measured using depth differences of hydrophones in each station. To get the radial and transverse components of the velocity relative to a specified direction, v_x and v_y are rotated based on azimuthal angle.

In this section, we compare the IMS hydroacoustic data from the 26 December 2004, Mw=9.1 Sumatra earthquake with seismograph data of the same event, available from Global Seismic Network (GSN) of the Incorporated Research Institutions for Seismology (IRIS). Given the large magnitude of this earthquake, clear arrivals were recorded by the hydroacoustic stations at very low-frequencies even though the hydroacoustic station data processing is not typically intended for these low frequencies. However, we have corrected the frequency response of the instruments, using the filter characteristics provided by CTBTO down to 0.1 Hz to be able to compare to the seismic station DGAR, so the results given here are recovered. Indeed, [64] have already

used these single hydrophone IMS data to produce an unclipped spectrogram of the combined earthquake and subsequent tsunami arrival. We converted hydroacoustic and seismic data to Seismic Analysis Code (SAC) format, and analyzed in SAC software [65]. Arrival times are calculated using the TauP toolkit, Flexible Seismic Travel-Time and Raypath Utilities [66]. Given earthquake information (event location, time, magnitude) and stations' location information, the TauP Toolkit embedded in SAC calculates arrival times of the body waves based on the earth-model embedded in the SAC toolbox.

2.3 Hydroacoustic vs. Seismic Data

2.3.1 Great Sumatra Earthquake

The study region is shown in Figure 2.2. The region $\sim$70km northwest of Diego Garcia is the Chagos Bank, the largest atoll structure in the world. The archipelago is a large bathymetric obstruction between northern stations, so signals observed at one triad might completely or partially be blocked at the other triad [67]. We have used data from these stations in the very low frequency regime over 0.01 - 0.05Hz band where the wavelengths of interest are above $\sim$30km. The depths of hydrophones at DGN station are 1248m, 1243m and 1182m, and at DGS station are 1413m, 1356m, and 1359m, respectively. To determine the vertical component of particle velocity, v_z, we have used two particular hydrophones that give the maximum depth difference at each station. The depth difference of the hydrophones are taken as 66 m at DGN station and 57 m at DGS station.

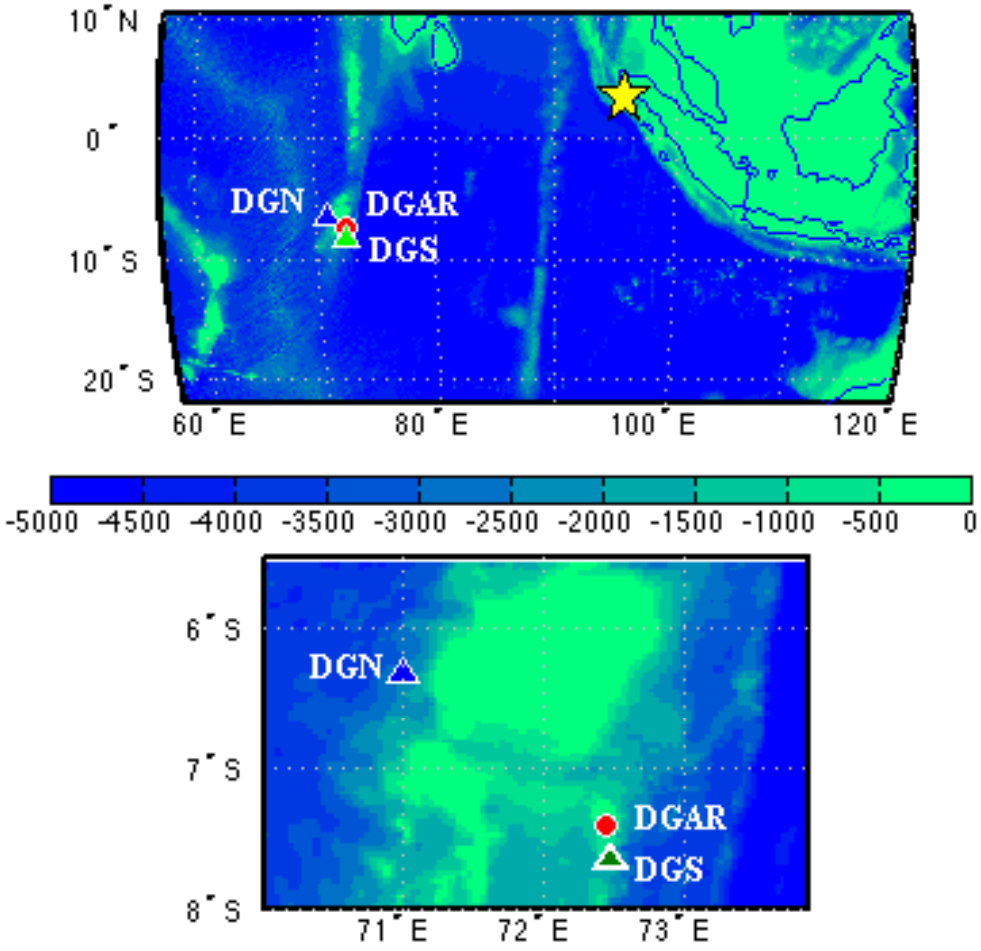

Figure 2.2: Maps of the study region using Smith and Sandwell bathymetry. Colorbar indicates seafloor depth in meters relative to sea level, with 500 meter contour intervals. a) Main shock of the Sumatra earthquake is symbolized with yellow star. Blue triangle indicates Diego Garcia North hydrophone triad, DGN (6.30S, 71.00E), green triangle indicates Diego Garcia South hydrophone triad, DGS (7.60S, 72.50E). Red circle labeled as DGAR (7.41S, 72.45E) is the seismic station on the Diego Garcia Island. The DGN, DGS and DGAR are located ∼2970 km, ∼2870 km, and ∼2865 km to the southwest of the earthquake location, respectively. b) Map of the Diego Garcia region in details. The DGN and DGS are located ∼200 km to the northwest and ∼25 km to the south of the DGAR, respectively.

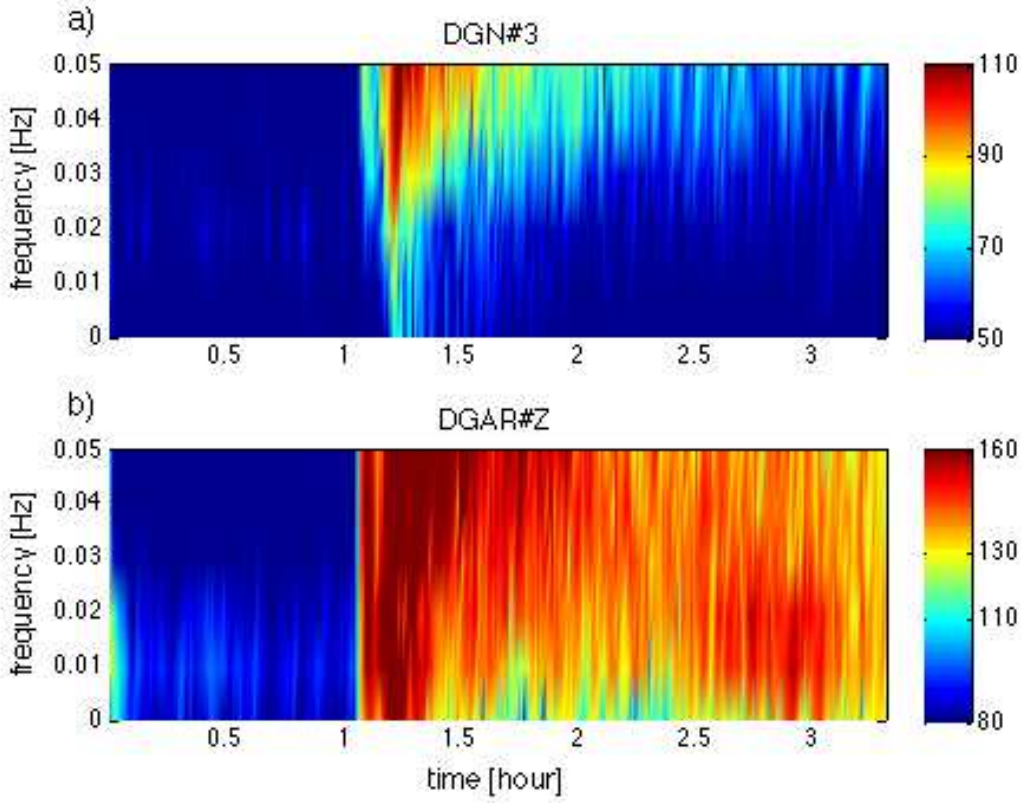

Figure 2.3: Spectrogram of a) the pressure recorded on the third hydrophone DGN (i=3) only b) the Vertical component of DGAR seismic station.

Figure 3 shows dynamic ranges of about 60 dB and 80 dB for the IMS station and adjacent seismometer station, respectively. This 20 dB difference in SNR indicates that the smallest earthquake detected by IMS station would be about one magnitude larger than for the seismic station.

2.3.2 Vector Sensor

Applying Eq (2.1) to hydroacoustic pressure data of f=0.01 - 0.05 Hz at DGN and DGS, we solve for three velocity components of the velocity v_x, v_y and v_z. The three velocity components are normalized to the maximum of each to compare to the seismic data of the same frequency band. Figure 2.4 shows radial, vertical and transverse velocities at both sites. Arrival times of *P* and *S* waves, calculated using the TauP toolkit, are indicated as black vertical lines on each time series.

Referring to Figure 2.4, Rayleigh waves are dominant in the radial and vertical components at $t = 800$ s - 1000 s for DGN, $t = 750$ s - 950 s for DGS, and $t = 750s - 950s$ for DGAR seismic station, and match each other very well. Moreover, one can see the same arrival cycles at $t = 750$ s - 850 s at both DGS and DGAR vertical components. Transverse components do not show a good agreement, which is consistent with the physics [62], that the water column only supports longitudinal waves, and transverse Love waves do not couple into the water column. The comparison is also consistent with the relative locations noting that DGS is much closer to DGAR than DGN is.

We have also generated synthetic mode seismograms to aid in the identification of seismic modes. The fundamental Rayleigh mode is large, as expected, arriving

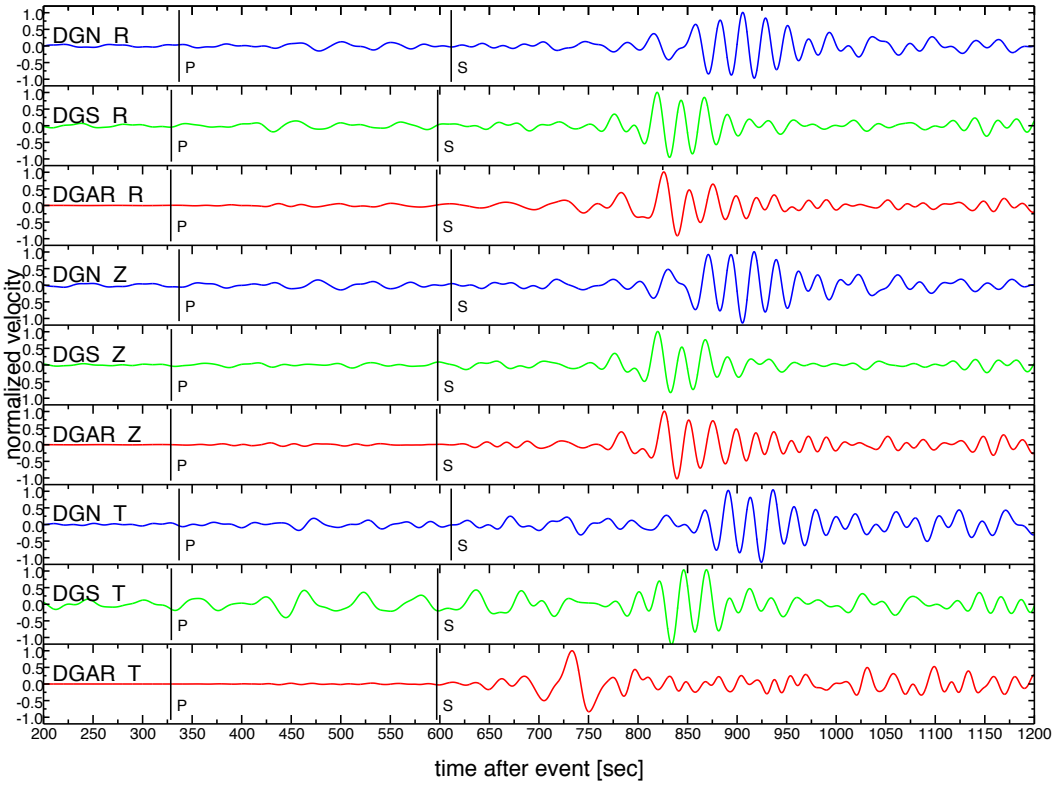

Figure 2.4: Hydroacoustic and seismic data of $f = 0.01 - 0.05$ Hz are plotted using Seismic Analysis Code (SAC). R: Radial, Z: Vertical, T: Transverse. Blue lines represent the DGN hydroacoustic data (top plots), green lines represent the DGS hydroacoustic data (middle plots), and red lines represent the DGAR seismic data (bottom plots). The x-axis corresponds to the time after event [200-1200 sec], y-axis corresponds to normalized velocity. Arrival times of P and S waves calculated using TauP are indicated as black vertical lines on each time series.

at DGAR at about 775 seconds (Figure 2.4). The synthetic seismogram for the one-dimensional preliminary reference earth model (PREM) using the Mineos programs [68], produces a fundamental mode of about 150 seconds in length. Adding 9 overtones yields a packet of about 75 seconds in length, preceding the arrival of the fundamental mode. The data (Figure 2.4) show a similar behaviour: the Rayleigh arrival is preceded by higher Rayleigh modes which are evident in the vertical components of DGS and

DGAR. The match between DGS and DGAR at the onset of the Rayleigh arrival is consistent with them being located within a wavelength of each other.

Looking at the DGAR transverse data (DGAR T) in Figure 2.4, the apparent transverse wave is significantly dominant at $t = 700s$ - $750s$, whereas the radial wave (DGAR R) is small in the same time window. We have performed a rotation analysis, an example of which is shown in Figure 2.5, where north-south (x) and east-west (y) components of both hydroacoustic and seismic data are first rotated over the azimuth angles $[180^\circ - 360^\circ]$ to determine the direction of maximum response that should be equivalent to the radial and transverse directions. Here, components rotated in each direction are called optimized radial, and components that are perpendicular to those are called optimized transverse. Then, the energy of optimized radial and transverse components at each direction are calculated at a specific time window, and compared to the energy of the data at the true source direction. In Figure 2.5 we show the results from one of the hydroacoustic stations, DGN, and the seismic station, DGAR. For optimized radial plots, the rotation analysis time window is $800 - 1000$ s for DGN, $750 - 950$ s for DGAR, where the Rayleigh waves are dominant. As expected, rotating north-south and east-west velocity vectors gives a maximum in optimized radial components, and minimum in optimized transverse components in both hydroacoustic and seismic station Figure 2.5.a and 2.5.b. For optimized transverse plots, the time window was $710 - 780$ s for DGN and $690 - 750$ s for DGAR. When the transverse Love waves are dominant, as in DGAR seismic station, the rotation result is reversed, so a minimum in optimized radial components and a maximum in optimized transverse components is seen (Figure

2.5.c). However, the same rotation process does not show significant change in the water column since we do not expect transverse coupling into the water column (Figure 2.5.d).

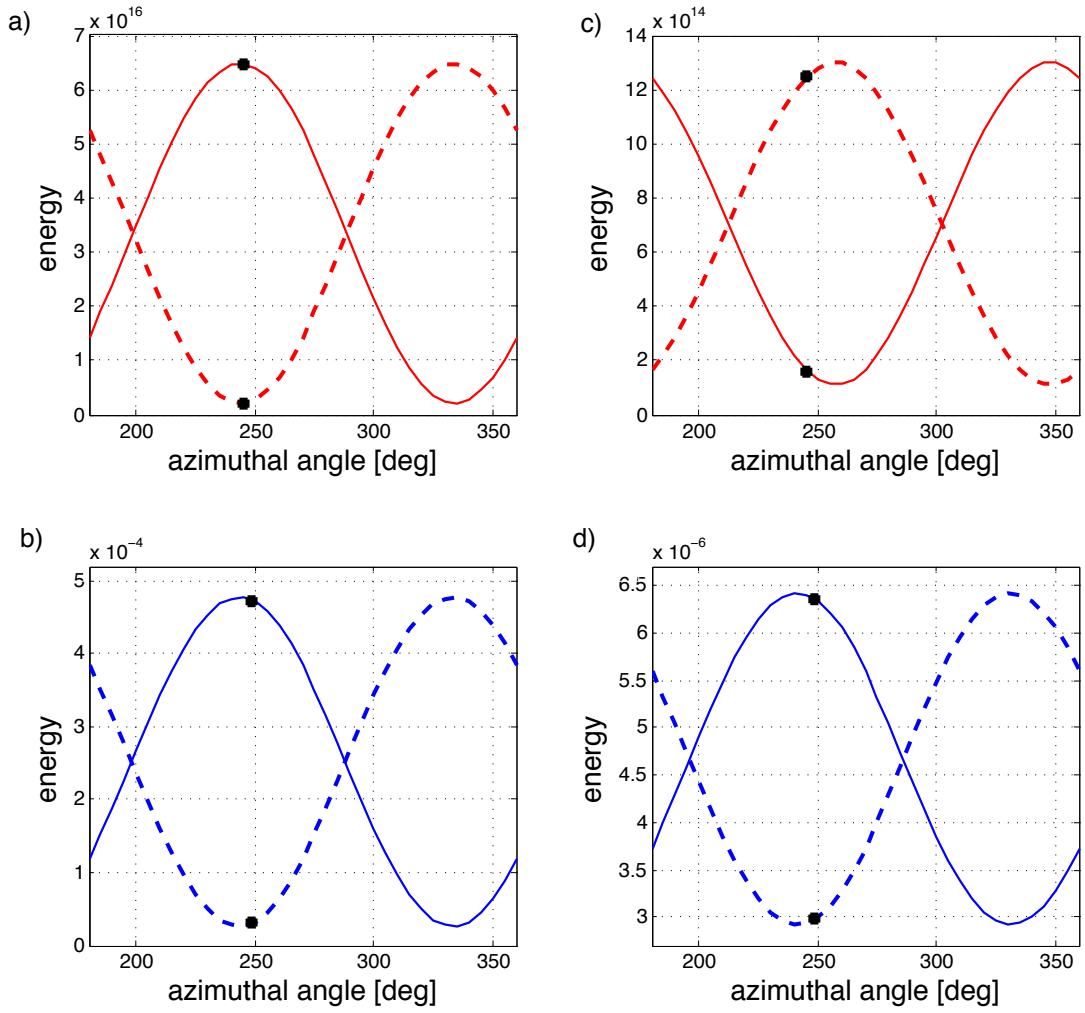

Figure 2.5: Optimized radial and transverse rotation results from DGAR (top plots with red lines) and DGN (bottom plots with blue lines). Continuous lines represent optimized radial, and dashed lines represent optimized transverse components.Black dots show the energy of the components at the true azimuthal angle. Radial rotation gives a maximum in radial component and a minimum in transverse component at both DGAR (a) and DGN (b). Transverse rotation results are reversed at DGAR (c), and do not show a significant change at DGN (d).

We have therefore demonstrated that hydroacoustic data at these low frequencies can be converted to seismic information. We can though, also obtain the directional information from a slowness analysis of one IMS triad pressure data that is consistent with earthquake location.

2.3.3 Directionality from slowness analysis

Previous work on slowness analysis of hydroacoustic data has been done in a higher frequency regime [8]. In this work, we perform a slowness analysis of hydroacoustic data over 0.01 - 0.05 Hz band at the *P*-wave regime using three pressure data at both DGN and DGS. The pressure data in Figure 2.6.a and 2.6.b indicate that the waveforms are the same in all three hydrophones and the predicted arrival times match the data. To localize the earthquake source location, delay times between each hydrophone pairs within a station are obtained from *pP* arrivals, which are well-identified because of their large signal to noise ratios (see Figure 2.6.c and 2.6.d). These time delays are used to determine horizontal slowness components (p_x, p_y) and estimate the azimuth to the source region using

$$t = \Delta p \tag{2.3}$$

where Δ is the geometric distance and t is the time difference between hydrophone pairs. This method [11] assumes that the wave front is a plane wave in the far field, and if the signals recorded at three sensors within a station are from the same source, the sum of time delays (t_{12}, t_{23} and t_{31}) should be close to zero, the closure relation. The measured

time delays for DGN are t_{12}=$-0.1s$, t_{23} =$-0.2s$ and t_{31} =0.3s, and for DGS are t_{12}=0.2s t_{23} =0s and t_{31} = $-0.2s$, and are indeed consistent with this closure relation.

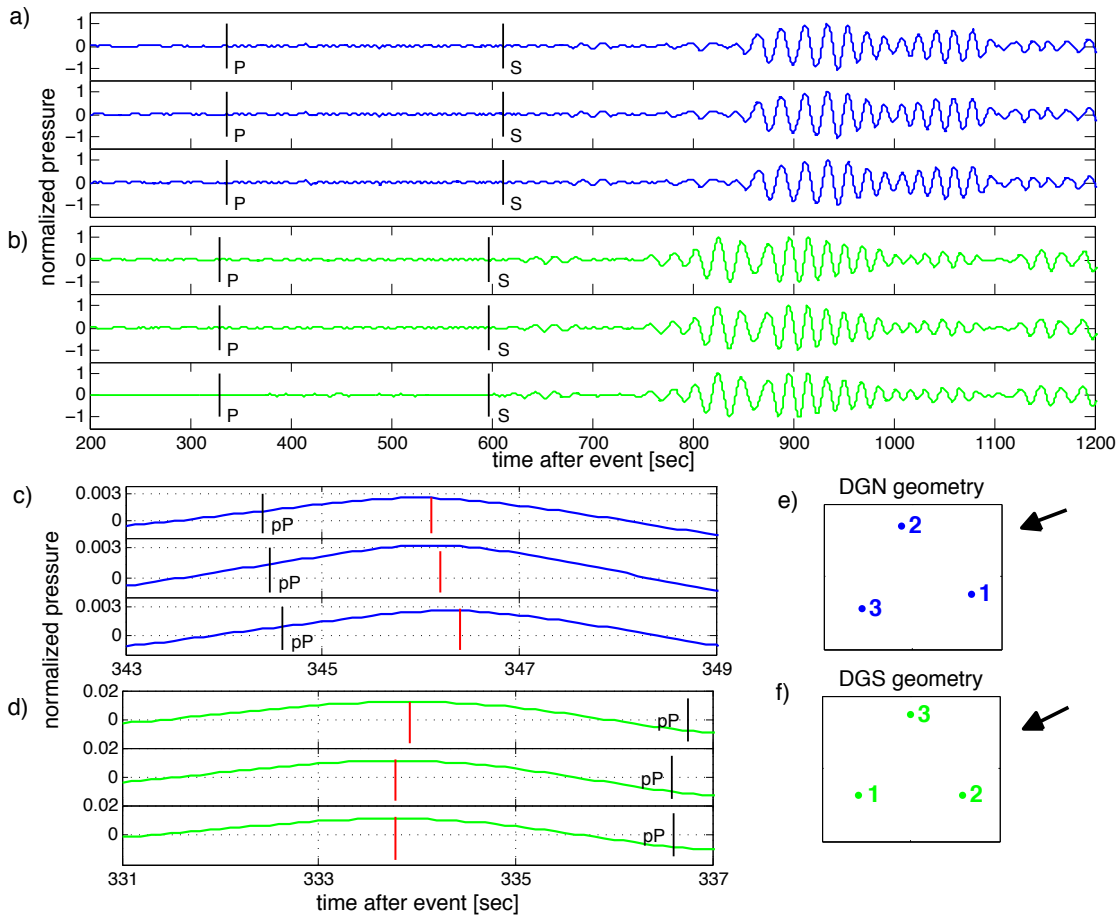

Figure 2.6: a) DGN (blue lines) and b) DGS (green lines) pressure data of f=0.01-0.05 Hz for hydrophones 1, 2 and 3, respectively. The x-axis corresponds to the time after event [200-1200 sec], y-axis corresponds to the normalized pressure. c) DGN *pP*-wave arrivals at [343-349] seconds and d) DGS *pP*-wave arrivals at [331-337] seconds. Black and red vertical lines represent the predicted and observed arrival times of pP waves, respectively. Orientation of hydrophones and source signal direction e) at DGN f) at DGS.

We have compared azimuthal angle obtained by slowness analysis with those predicted by SAC. From slowness analysis, the direction of propagation at the DGN and

DGS are found to be 0.9° and 2.4° off from the direction predicted by SAC, respectively. The orientations of DGN, DGS, and source signal directions are shown in Figure 2.6.e and 2.6.f.

2.4 Conclusion

We analyzed records of the Sumatra Earthquake of 2004 from two IMS hydrophone stations and a nearby GSN island station in the very low frequency band (0.01-0.05 Hz). The hydroacoustic data were successfully converted to vector velocities comparable to seismic data. A spectral analysis of hydroacoustic and seismic data indicated that the magnitude of the smallest earthquake detectable by the tested IMS stations would need to be about one order of magnitude larger than what a conventional seismic station could detect. Vector sensor emulation from IMS hydrophone triads have shown to give essentially the same results as seismic data in radial and vertical motions at an adjacent land seismic station. Consistent with the physics, transverse Love waves in the water column do not couple whereas *P* waves and Rayleigh waves with radial and vertical motion do couple. A slowness analysis based on longitudinal propagation physics in the water column permits the determination of the direction of the source location at a single IMS triad.

2.5 Acknowledgments

We thank Mark Prior for providing access to hydroacoustic data collected by the Comprehensive Test-Ban Treaty Organization's International Monitoring System (CTBTO-IMS) and Mario Zampolli for providing frequency response characteristics of hydroacoustic stations. Information on the procedure for distribution of IMS data and data bulletins to Member States can be found at: [http://www.ctbto.org/verification-regime/the-international-data-centre/distribution -of-data-and-data-bulletins-to-member-states/]. Seismic data were retrieved from the Global Seismograph Network (GSN) via Incorporated Research Institution for Seismology (IRIS). We also would like to thank the reviewers for their detailed comments that helped improve the original manuscript.

Chapter 2, in full, is a reprint of the material as it appears in the Geophysical Research Letters. Selda Yildiz, Karim Sabra, LeRoy M. Dorman, W. A. Kuperman, "Using hydroacoustic stations as water column seismometers", GRL, Vol. 40, 2573-2578, doi:10.1002/grl.50371, 2013.

Chapter 3

Target localization through a data-based sensitivity kernel : A perturbation approach applied to a multistatic configuration

A method to isolate the forward scattered field from the incident field on an object in a complex environment is developed for the purpose of localization. The method is based on a finite-frequency perturbation approach, through the measurement of a data-based sensitivity kernel. Experimental confirmation of the method is obtained using a cylindrical tank and an aggregate of ping-pong balls as targets surrounded by acoustic sources and receivers in a multistatic configuration. The spatial structure of the sen-

sitivity kernel is constructed from field data for the target at a sparse set of positions, and compared with the expected theoretical structure. The localization of one or a few targets is demonstrated using the direct-path only. The experimental observations also show that the method benefits from including later arrivals from the tank wall and the bottom/surface reverberation, which indeed enhance the localization.

3.1 Introduction

In underwater acoustics, sonar networks have received attention in terms of their use for target detection and localization [25, 26, 27, 28]. While bistatic and multistatic approaches have received attention due to separated receiver geometry, multistatic configuration enhances the performance of target detection and localization by increasing the survey coverage rate and providing a range of scattering angles for a given target by exploiting spatial diversity [29]. Further details on the comparison of sonar systems can be found in Kim et al [28]. In general, as the back-scattering cross-section of a target is weak, the source signal for monostatic sonar needs to be loud enough to make the backscattered echo emerge from the ambient noise. Detection of a target by exploiting its forward scattering is then of interest, as the echo amplitude is higher than in back-scattering. Nevertheless, it is difficult to separate the forward scattered signal from the directly arriving beam coming from the source; i.e. often referred to as “looking into sunlight problem“ [30, 31]. In this study, by taking advantage of the large forward scattering cross section, a data-based method is developed to localize an object in a

complex environment using a multistatic configuration. The method is based on a perturbation approach between with and without object, through the amplitude sensitivity kernel measurements.

The difficulty of separating the forward scattering from the direct-arriving beam has been addressed in an acoustic barrier problem using a time reversal mirror [32], the advantage of time-reversal being to account for the reverberation and scattering from the boundaries that often limit sonar performance in a shallow-water configuration. Further experimental work investigated a time-reversal-based forward-looking technique for an acoustic barrier problem in a scaled environment that was representative of harbor configurations [69]. As time-reversal produces a stable focus, the goal was to detect a target crossing a plane defined by vertical source−receiver arrays, by measuring the slight change in the low-amplitude side lobes outside the focal spot; e.g. to detect submerged objects that enter the field of view of a system in a harbor. The technique was implemented with broadside ensonification (no time reversal) and with time reversal. With time reversal focusing, the passage of the target in the field of view can be seen whereas broadside ensonification does not discern the passage. Also, using time reversal, target detection and localization was performed from a back-scattering configuration using the decomposition of the time-reversal operator (DORT) method of Prada et al. [70], after initial tests in a pool basin [71, 72]. Note that another study used time reversal for the detection and localization of a target on the seafloor in the presence of bottom scattering using laboratory-scale data [34].

Finally, the acoustic barrier problem was recently investigated in shallow-water

by looking at the shadow effects on a set of eigenrays associated with the presence of a target. Two vertical source and receiver arrays were used to identify the eigenbeams where their forward- scattered intensity was modified by the target. Depending on the number of perturbed eigenbeams, the target localization was achieved using a forward or inverse problem [35, 36]. The practical disadvantage of this approach is the requirement for two well-sampled source and receiver arrays that provide a two-dimensional localization that is limited to the plane defined by the arrays.

The main focus of the present study is to use a multistatic configuration and a data-based method to localize a target in three dimensions without the use of an accurate propagation model, by taking advantage of the large forward scattering cross section. The idea is not to work on the separation of the forward scattering from the direct path, but rather to focus on the amplitude change in the direct-path signals between without and with the perturbation (the target) in the medium. There is no need to use loud sources anymore, as the direct-path signals features high power. Furthermore, by using a set of multiple sources and receivers surrounding the target, the performance of the method is greatly increased. In the absence of a model, the medium is spatially sampled to build a data-based model that will be used to back-project the data. In a multistatic configuration, this spatial sampling can be performed by a moving active source that is surrounded by receivers in the medium, or by moving a passive target between a set of sources and receivers, as is used in this study. These approaches do not require any prior information or estimation of the medium properties.

The methodology consists of a perturbation approach to locate a local change

in the medium. By measuring the amplitude change of the direct path without and with the target in a multi-static configuration, a linear inverse problem is constructed whereby the solution is the target position. This approach requires a sensitivity kernel (SK) analysis [37] for the propagation medium between each source and receiver pair. In general, SKs are used to define the relationships between a change in the acoustic field and a local change in the medium. In underwater acoustics, SKs have been used in travel time tomography [38], for local changes in density [36] and sound speed [39], and for surface scattering in a waveguide [40]. In the present study, the SK between a set of sources and receivers is measured experimentally, which determines the perturbation in the acoustic field as a function of a local perturbation at a target position that is associated with the direct arrivals [43]. The target used in this experiment is an aggregate of ping-pong balls, and the SK is obtained by the measurement of the difference in the scattered field without and with the aggregate inside the cavity, with the positions of the sources and receivers fixed, and at the periphery of the tank. The SK derived from the difference between the two fields is used to localize the target at any position within the measurement region. Having implemented the method using the direct arrivals, we have also observed experimentally that this approach obtains benefit from the inclusion of later arrivals, which indeed enhances the results.

This paper includes four sections. Following this Introduction, Section II introduces the experimental set-up and the theoretical and experimental representations for the SK spatial structure. Section III presents the linear inversion method, and shows the localization results. The paper then continues with a discussion on the use of later

arrivals in this reverberating medium, followed by conclusions.

3.2 Experimental results

Fig. 3.1(a) shows the experimental set-up that comprises a fish tank of 5.6 m in diameter and a water depth of 1.05 m. The source and receiver transducers are located on a sensor cable of 5.2 m diameter, and the depths of the sensors vary between 0.2 m and 0.8 m. There are eight sources, where the inter-element spacing is approximately 2 m, and 16 receivers, where the inter-element spacing is approximately 1 m. The target is an aggregate of four ping-pong balls that are identical with a 2 cm radius, and it floats at about a depth of 0.5 m. The aggregate is tied to a metal weight using a fishing line and the weight lies at the bottom of the tank. The target is successively shifted on a 13x13 square grid at the center of the fish tank, with 10 cm grid spacing, which defines the SK region. With the completion of 13x13 = 169 grid-point measurements (Fig. 3.1(b) circles), the target is moved to three random positions (Fig. 3.1(b) triangles) that are in-between the grid points of the SK region. Here, to help the reader, the measurements on the grid points are referred to as the *on-the-grid* points and the measurements in-between the grid points are referred to as the *off-the-grid* points.

The central frequency of the transducers is 10 kHz (wavelength $\lambda = 15$ cm) with an 8 kHz frequency bandwidth, and the sampling frequency is $Fs = 100$ kHz. The SK analysis consists of the measurement of the difference between a perturbed field and a reference field. Here we call the reference field and the perturbed field as the fields

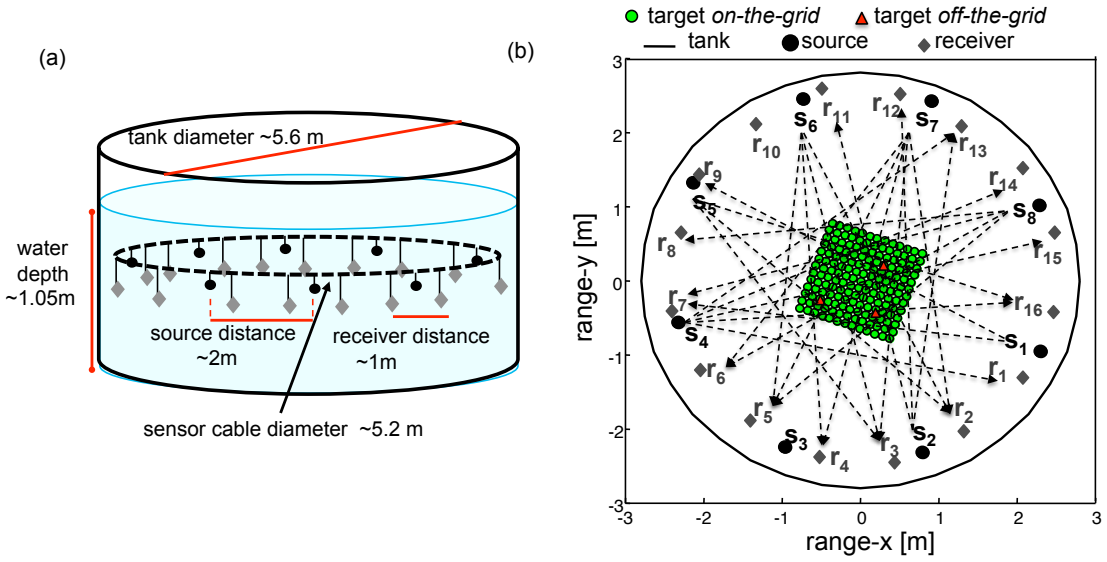

Figure 3.1: (color online) (a) Experimental set-up, with a tank of 5.6 m in diameter and a water depth of 1.05 m. The set-up includes eight sources with $\sim$ 2 m inter-element spacing and 16 receivers with $\sim$ 1 m inter-element spacing. The depth of the sensors vary between 0.2 m, and 0.8 m. b) The source−receiver geometry and the grid sampling area in the tank. The circles show the measurements of the 13x13 = 169 sampled region for the SK analysis. The triangles show the positions in-between the grid points that are to be localized. The multistatic configuration of the sources and receivers used in this experiment enhances the target detection and localization, and the pairs used for the localization are shown with the connecting dashed lines.

before and after a perturbation in the medium, respectively. The reference field is when there is no target in the tank, and the perturbed field is measured in the presence of the target, where the recorded signals include the echoes scattered by the target and also the echoes reflected from the tank boundaries. In practice, the acoustic echoes due to the fixed tank boundaries remain identical and vanish after subtraction, whereas the echoes that interact with the target change with respect to the positions of the target, and participate in the SK measurement [73, 74].

Signal acquisition starts with the target being at the first position of the 169-sampled grid. A two period pulse is generated at source s_1 while a time series composed by the echoes is recorded on all of the 16 receivers (see Fig. 3.1(b) for the geometry of the system). Having completed the acquisition between source s_1 and receivers r_{1-16}, the same pulse is transmitted from all of the other sources, respectively. One round of signal acquisition, with transmission between eight sources and 16 receivers, takes 5 s, which is referred to here as one *shot*. After a set of four *shots* is completed (20 s), the target is moved to the next position. The acquisition is repeated every time the target is moved to a successive position until the completion of 169 *on-the-grid* points. Signal acquisition is repeated for all of the *off-the-grid* points in the same order. Here, for the perturbed field measurements, signal acquisitions are averaged over four successive shots. As no trustful measurements were performed in the absence of the target during the course of the experiment, the reference field is estimated by using a moving-average technique, which is based on taking an average of perturbed field realizations for a given source-receiver pair at successive target positions. By averaging

the signals obtained from different target positions, the target echoes and the echoes reflected from the tank due to the target are diminished, and only echoes due to the fixed tank boundaries remain, as if there was no target inside the tank. When the target is small, the moving-averaged field is only an estimate of the exact referenced field which may still be appropriate if the average is made for a large number of target positions [73]. In practice, the reference field is estimated from an average of 20 successive target positions; this number of realizations was chosen based on the 15-min maximum stability time of the medium.

In Fig. 3.2, a sample of the reference field, perturbed field and the subtracted field is shown between source s_1 and receiver r_6 for a given target position in the sampled region. Although, the subtracted field appears to be very small compared to the reference field, due to the change of the target position, the information embedded in it contains sufficient spatial information to be used for localization purposes. Indeed, the spatial structure of the subtracted field is shown in Fig. 3.3, which is calculated for a source−receiver pair and a set of target positions. Each horizontal line of Fig. 3.3 corresponds to a sample of the subtracted field, as in Fig. 3.2. The next step is to take the relative amplitude difference for all of the 169 positions at the time of the direct path arrivals for a given sensor pair and calculate the spatial structure of this experimental SK. Here, we have preferred taking amplitude perturbations over travel time perturbations as the changes in amplitudes are (1) more pronounced than the changes in travel-time for a local density perturbation (as for a target) and (2) more robust to environmental fluctuations, e.g., temperature change in the tank.

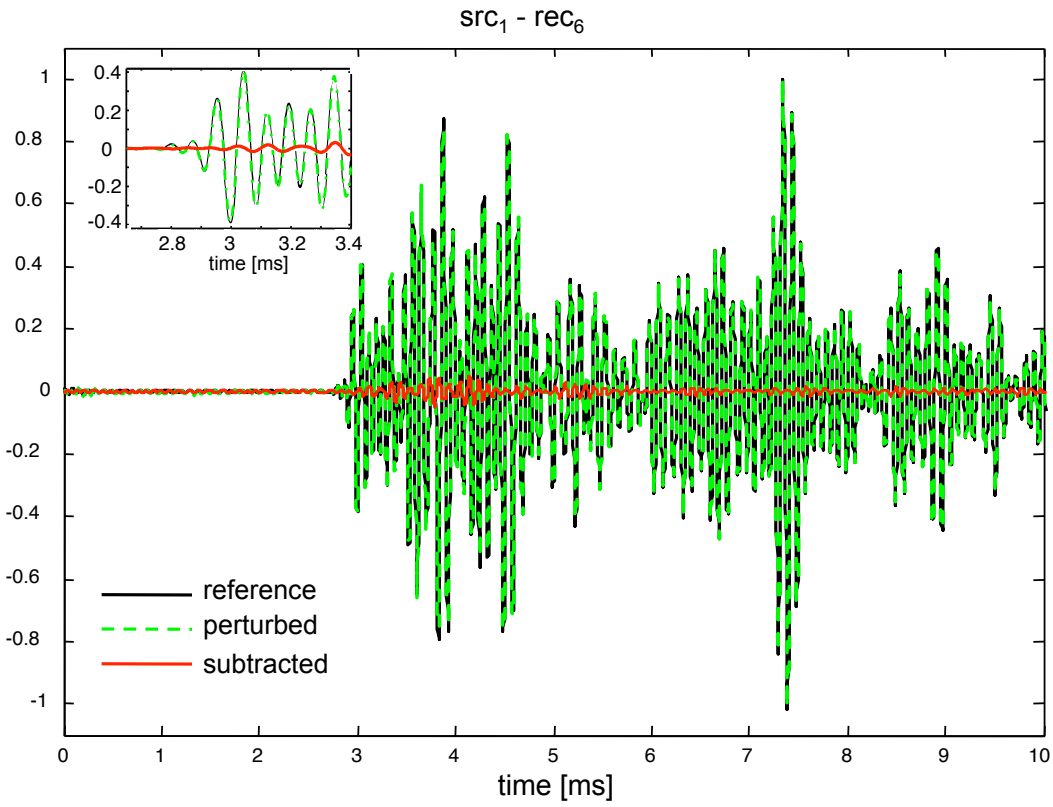

Figure 3.2: (color online) The reference field, the perturbed field *versus* the subtracted field between source s_1 and receiver r_6 for a given target position *on-the-grid*. All three of these fields are normalized with respect to the reference field. The SK analysis requires the amplitude difference between the perturbed field and the reference field at the time of the direct path. This amplitude difference is of the order of a few percent for any source−receiver pair, an example of which is shown in the enlarged plot in the inset with a time window of $t = 2.65 - 3.4$ ms.

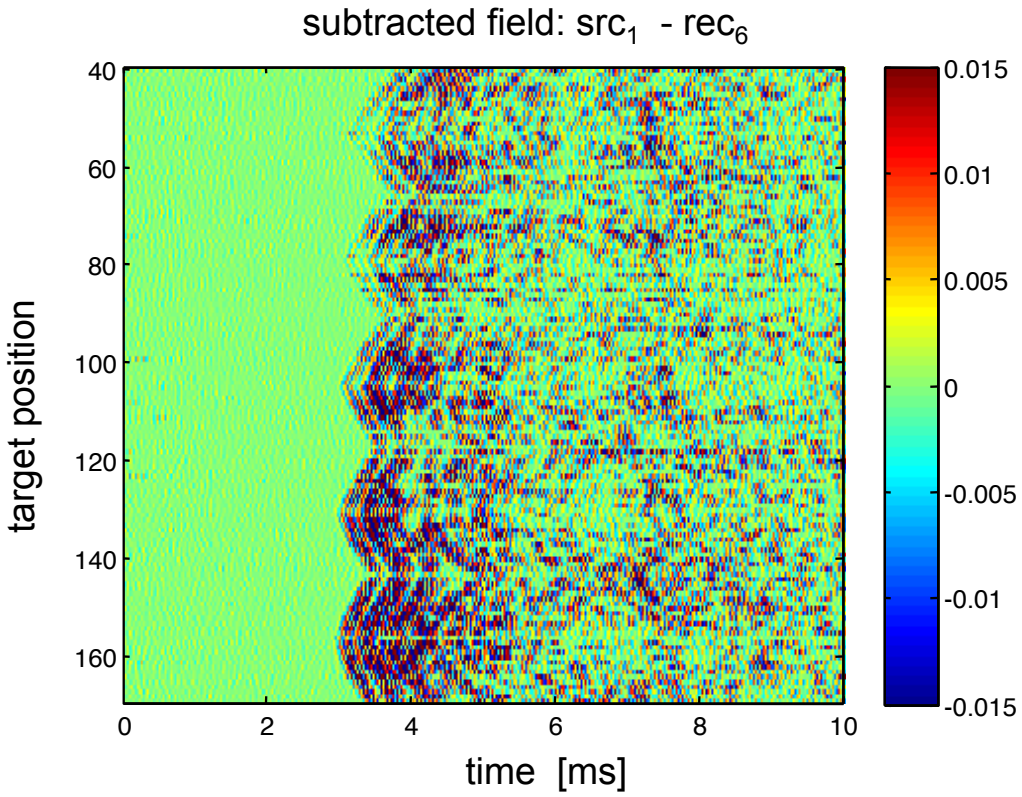

Figure 3.3: (color online) The subtracted field between source s_1 and receiver r_6 for a subset of *on-the-grid* target positions. The subtracted field is normalized with respect to the reference field, as in Fig. 2. Although it is very small in amplitude, the subtracted field provides spatial information according to the target position for a given source − receiver pair. The triangle shape associated to the first arrival is due to target scattering and it carries the signature of the data-based SK projected on the 13x13 sampled region.

A comparison of the experimental and theoretical SKs is shown in Fig. 3.4. The theoretical SK expression here is derived from the perturbation theory in the first-order scattering Born approximation. For a local sound speed change in a unit volume of $\delta V = 1$ m^3 at position r', the SK is traditionally formulated between a source in r_s and a receiver in r_r as [38]:

$$Q(\omega; r_s, r_r, r') = -2k^2 G(\omega, r_s, r') G(\omega, r_r, r') \tag{3.1}$$

where k is the wavenumber and $G(\omega; r_s, r')$ [and, respectively $G(\omega; r_r, r')$] are the Green's function between r_s and r' [respectively, between r_r and r'] at frequency ω. The SK is defined as the product of the two Green's functions from the source/receiver to the perturbation, which is the target location here. In the case of a target with density change, a generalized SK can be defined as [36]:

$$\tilde{Q}(\omega; r_s, r_r, r') = -4\pi f_\infty(w, \varphi_s + \varphi_r) G(\omega; r_s, r') G(\omega; r_r, r') \tag{3.2}$$

where f_∞ represents the scattering form function which is a function of the target properties, scattering angles φ_s and φ_r [as defined in Fig. 3.4], and the frequency ω.

Applying the inverse Fourier transform, for the source spectrum $P_s(\omega)$, the acoustic pressure field perturbation in the time domain becomes [43] :

$$\triangle P(t; r_s, r_r, r') = -\frac{1}{2\pi} \int_{\infty}^{\infty} 4\pi f_\infty(w, \varphi_s + \varphi_r) G(\omega; r_s, r') G(\omega; r_r, r') P_s(\omega) e^{j\omega t} d\omega \tag{3.3}$$

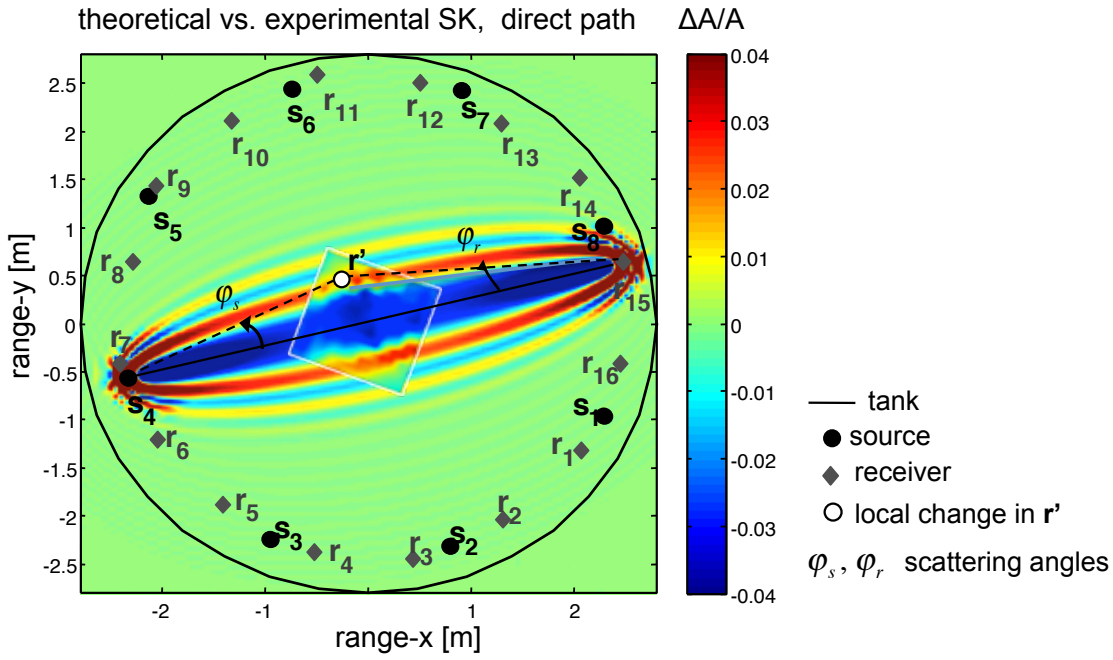

Figure 3.4: (color online) The theoretical and experimental SK spatial structure associated with the direct path between source s_4 and receiver r_{15} with a schematic of the scattering angles φ_s and φ_r between the given source−receiver pair and the local change in r'. The theoretical SK is calculated using the perturbation theory in the first order scattering the Born approximation within the whole tank region, whereas the experimental SK is computed within the measurement region of 13x13 *on-the-grid* points (delimited by the white square). The SK spatial structure shows diffraction-based oscillations around the Fresnel zone in free space. The SK measurement becomes a potential approach for a liner inversion to locate a target due to its spatial sensitivity along and outside the ray-path region.

which can then be formulated to be compared to the experimental SK results in Fig. 3.4, as in [Roux et al] [43]:

$$\frac{\triangle A}{A} = \frac{\triangle P(t_i; r_s, r_r, r')}{P(t_i; r_{s,} r_r)} = -4\pi \frac{\int_\infty^\infty f_\infty(w, \varphi_s + \varphi_r) G(\omega; r_s, r') G(\omega; r_r, r') P_s(\omega) e^{j\omega t_i} d\omega}{\int_\infty^\infty G(\omega; r_s; r_r) P_s(\omega) e^{j\omega t_i} d\omega} \tag{3.4}$$

Here, t_i is the direct travel-time at when the reference field, $P(t_i; r_{s,} r_r)$, is maximum within the direct arrival for a specific source−receiver pair. The amplitudes of both the reference and the perturbed field at this time are used to calculate the relative amplitude change $\triangle A/A$, as a function of the perturbation position in r'. Eventually, $\triangle A/A$ is computed for all of the perturbation locations to obtain the spatial structure of the SK. As we limit ourselves so far to the direct field, the Green's functions are calculated in a homogeneous medium.

Unlike the SK physics, Eq. 3.4 shows the nonlinearity of this perturbation problem due to the form function, f_∞, which has a nonlinear dependence on target properties characterized by its mass density, size, and longitudinal and transverse wave speed. That is, f_∞ will be different for given different targets. However, we here limit ourselves to the SK measurement in the presence of the same target, and the localization problem will also be investigated with the same one, which turns the problem back into a linear one.

The experimental SK is computed by measuring the $\triangle A/A$ for the target at each of the 169 grid points, for a given source and receiver pair. Note here that the experimental SK is computed only within the SK region that includes 169 measurement

points, whereas the theoretical SK is computed within the whole tank with the same grid separation used in the experiment.

Both of the SKs, calculated between source s_4 and receiver r_5, are shown in Fig. 3.4, where the experimental SK is overlapped on the theoretical one. The experimental results confirm the spatial structure within the experimentally sampled region. The SK spatial structure here corresponds to typical diffraction-based oscillations around the Fresnel zones in free space, which shows the spatial sensitivity along and outside the ray path between the sensor pair. This spatial structure of connecting the points within the region makes the SK approach a linear approach for inversion, as aside from its straightforward use in the forward problem, the sensitivity kernel is also used to invert for the environmental changes [41, 42, 39]. Having obtained a good match between the theoretical and experimental SKs, we have investigated the forward problem. We now use the formulation of a linear inversion, to explore the localization of the *off-the-grid* targets through the SK analysis.

3.3 Target localization performed with linear inversion

In this section, we demonstrate a data-based SK. The inversion problem can be defined as a linear set of equations for each source−receiver pair, within the Fresnel zone, discretized with respect to the unknown target position r' that should belong to the

sampled SK region as [36]:

$$\frac{\triangle A(t_i; r_s, r', r_r)}{A(t_i; r_s, r_r)} \approx F(t_i; r_s, r', r_r) p(r') \tag{3.5}$$

with local perturbation here being a quantitative indicator of the target presence at position r', $p(r')$, instead of the sound speed and the density as in Marandet et al [36]. F is the Born-Frechet kernel that is defined as

$$F(t_i; r_s, r_r, r') = \frac{\int d\omega \tilde{Q}(\omega; r_s, r_r, r') P_s(\omega) e^{j\omega t_i}}{\int d\omega G(\omega; r_s, r_r) P_s(\omega) e^{j\omega t_i}} \tag{3.6}$$

and it connects the relative amplitude changes to the quantitative indicator of the target position. In the present study, we benefit from the multistatic configuration that provides a large set of source$-$receiver pairs (r_s, r_r) that satisfy Eq. 3.6. The inversion problem can then be formulated as a linear inverse problem, as:

$$\frac{\triangle A}{A} = F\,\boldsymbol{p} \tag{3.7}$$

The column vector $\triangle A/A$ corresponds to the data of a particular unknown target position that is located in the sampled region but *off-the-grid* and $\boldsymbol{p}$ represents the position vector of that particular target to be localized. F is the SK matrix that defines the pressure field perturbations on the sampled region for all of, or for a subset of, the source$-$receivers pairs. By measuring the pressure field perturbations only *on-the-grid* points for given set of source$-$receiver pairs, here represented by F, we explore the indicator of the target

presence in-between the grid points, which is defined by $\boldsymbol{p}$.

To build the F matrix, the relative amplitude change $\triangle A/A$ is computed for the target at each one of the 169 *on-the-grid* points, which then form one row of SK matrix F,

$$F_1 = \left[\triangle A/A_{s_1,r_1,n1} \quad \triangle A/A_{s_1,r_1,n_2} \quad \triangle A/A_{s_1,r_1,n_3} \quad \ldots \quad \triangle A/A_{s_1,r_1,n_{169}} \right] \tag{3.8}$$

where s_1 and r_1 represent the source and receiver index numbers, respectively; and n corresponds to target position r', and represents the index number of the positions within the 13x13 sampled region. Having done the same process for all sensor pairs, or a subset of them, the vertically concatenated F matrix is formed. In the case when using M sources and N receivers for inversion, the F matrix has the size of [(M x N) x 169] and the form of:

$$F = [F_1; F_2; F_3; ...; F_{MN}] \tag{3.9}$$

where F_1 is the first sensor pair, F_2 is the second, and so on, with F_{MN} being the last sensor pair used. After obtaining the F matrix, the relative amplitude change using the very same sensor pairs is derived for an unknown target position to be located, which is represented by the data vector $\frac{\triangle A}{A}$. In Eq. 3.7, to invert for $\boldsymbol{p}$, we need an estimation of F^{-1} which we obtain from a singular value decomposition (SVD) of F: $\tilde{F}^{-1} = V\tilde{S}^{-1}U^t$ with U and V as unitary matrices, and S as a diagonal matrix with diagonal values ordered as singular values. In the present study, only a subset $L \sim 80$ of the first singular values are kept based on an empirical threshold, which is obtained from the

optimal localization results. Then, $\widetilde{S}^{-1}$ is a diagonal matrix with L non-zero elements and $\widetilde{S_i}^{-1} = \frac{1}{S_i}$ for $i \in [1, L]$.

The comparison between the experimental and theoretical SK revealed similar spatial structures (Fig. 3.4). The target localization could then be made using either one or the other. As the main focus of this study is to demonstrate the use of data-based SK that does not require a priori information of the medium, the inversion process is first performed on the experimental SK for the direct arrivals. The sensor pairs are chosen based on the resolution of the SK spatial structure that they provide in the investigated area at the center of the tank. Ultimately, the amplitude change in the direct path due to target location makes the use of the SK meaningful, with the pairs providing forward scattering. The results shown here are calculated using a set of 26 sensor pairs, which are shown in Fig. 3.1(b) with the dashed lines connecting them.

The localization results when the target is at three different *off-the-grid* positions are shown in Fig. 3.5(a-c). The target position is retrieved successfully with a probability of presence reaching 0.25, while some side lobes around 0.1 still pollute the inversion result.

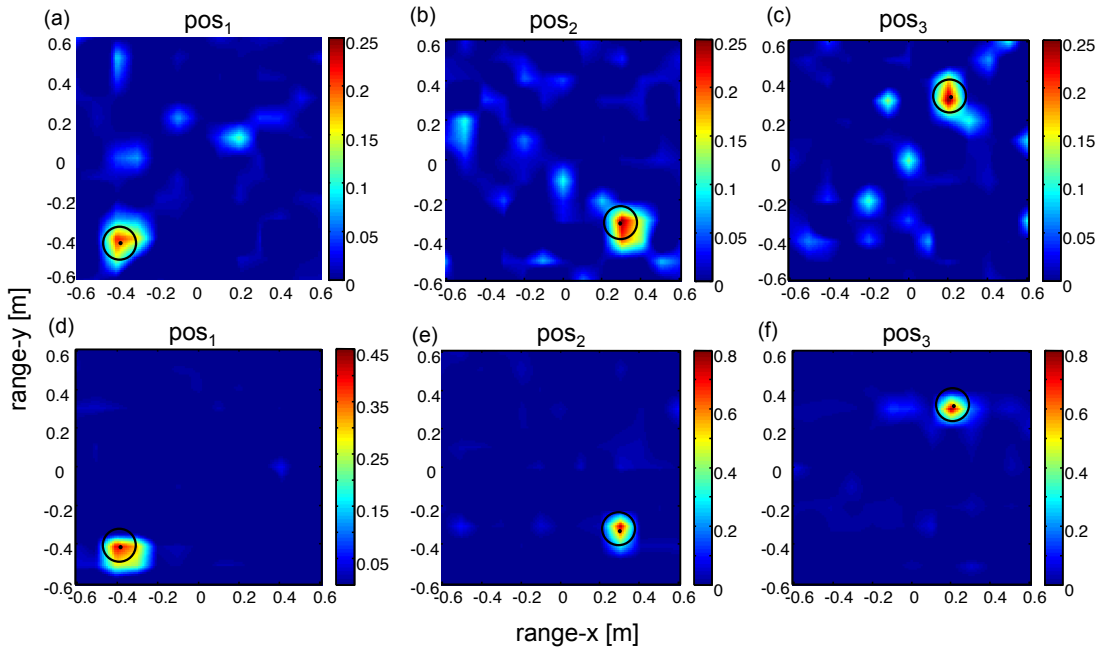

Figure 3.5: (color online) The localization using the direct path arrivals when the target is at three different *off-the-grid* points, with the probability of presence reaching 0.25 for all three positions: (a) pos_1, (b) pos_2, (c) pos_3. The localization when the later arrivals are also included for the same positions with the probability of presence reaching 0.45 for pos_1 (d), 0.8 for pos_2 (e) and pos_3 (f). Including later arrivals, up to $t = 5.5ms$, increases both the resolution and the contrast between the signal and the background.

3.4 Discussion

This section investigates the possibility to improve the inversion results by including the later arrivals associated with the tank reverberation, following the same methodology. In practice, it is not known whether the direct SK problem is correct or not within the late arrival regime, as the SK spatial structure cannot be modeled for such a reverberating medium. Nevertheless, looking at the subtracted field for a specific source−receiver pair in Fig. 3.3, one can see that the triangle shape associated with the spatial structure of the 13x13 sampled region of the direct arrival SK (at $t =\sim 3.5$ ms) preserves some spatial structure for later arrivals up to $t =\sim 5.5$ ms. As the SK analysis was performed with data only, in the formulation of the forward problem, we can always include some $\frac{\triangle A}{A}$ that are associated with the later arrivals for each source−receiver pair and the corresponding data-based F, as sampled *on-the-grid*. Although the amount of the later arrivals giving such spatial information, hence to be used in inversion, is different for each source−receiver pair, we here use the same time window for each pair for the sake of simplicity. With this aim, we now use the later arrival times up to $t = 5.5$ ms for localization of the target position, and show that the results get better not only in terms of resolution but also in terms of the contrast between signal and background, with a probability of presence reaching 0.45 for the position pos_1, and 0.8 for positions pos_2 and pos_3 as in Fig. 3.5(d-f).

The decision for the picking of the number of the arrivals for improved localization can be made based on the a-posteriori peak-to-noise ratio, which is calculated as the

maximum value of the pixel of the localization image divided by the standard deviation of the rest of the image pixels, excluding the maximum value. Note that only one target at an unknown position is used during this experiment. However, as the formulation of the inverse problem is linear, we can apply the principle of superposition for multitarget localization. As the targets are in the far field from each other, we can neglect the multiple scattering contribution among them. In this case, the SK matrix F in Eq. 3.7 remains the same, whereas the data vector $\frac{\triangle A}{A}$ is now calculated from the sum of the perturbed fields for all of the targets to be localized. Fig. 3.6 shows the multi-target localization for the three positions of the target, which were shown separately in Fig. 3.5. As for the separate target case, the method also benefits from including later arrival times up to $t = 5.5$ ms, with the use of the data-based SK analysis.

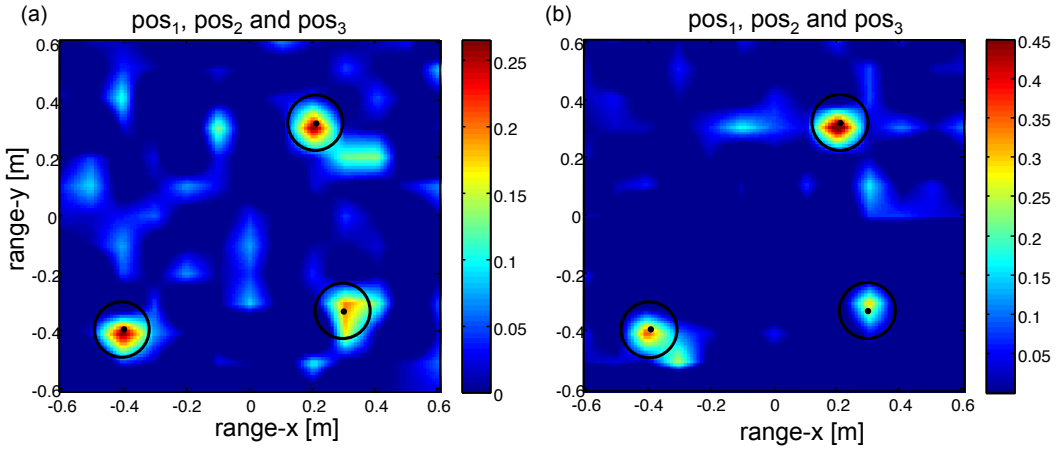

Figure 3.6: (color online) Using the principle of superposition, synthetic data is created for multi-target localization. The localization of the three targets, as used separately in Fig. 5, is shown by (a) using only the direct arrivals (b) including also later arrival times up to $t = 5.5ms$.

As explained previously, we have used a moving-average method to overcome the environmental fluctuations during this SK study (a few hours in total). The stability

time was ~ 15 min for the later arrivals and much longer for the first arrivals. Depending on the use of early or late arrivals to localize the target, the localization result will degrade more or less fast. When the environment changes rapidly, the solution to maintain the resolution of the inversion result is then to increase the number of source-receiver pairs and limit the analysis to the direct path between each pair. Additionally, as well as investigating the method's performance for different targets in size and shape, taking the vertical dimension into account by sampling the SK for a target on horizontal grids at different depths could be the ambition of future works. In the present paper, the main focus was to demonstrate the use of the amplitude change of the direct path arrivals as a proof of concept of a data-based forward-scattering localization technique.

In conclusion, the experimental data obtained in a reverberating tank were analyzed using a data-based sensitivity kernel method. The experiment involved measurements with a target located at a set of grid points inside the tank. The relative amplitude change between the reference and the perturbed fields for the direct path between an ensemble of source$-$receiver pairs is used for the calculation of a data-based SK, which provides the ingredients for the forward problem solution. Having shown that the experimental and theoretical SKs agree, the SK analysis is applied to the target localization. This method is demonstrated for single and multi-target cases using first arrivals. We have also shown that the addition of later arrivals improves both single and multi-target localization results, not only in the contrast but also in the resolution of the localization result.

3.5 Acknowledgments

This project is funded by the Office of Naval Research (ONR). Christian Marandet was supported by the Groupe d'Etudes Sous-Marines de l'Atlantique (GESMA), Direction Generale de l'Armement (DGA).

Chapter 3, in full, is a reprint of the material as it appears in the Journal of the Acoustical Society of America. Yildiz S., P. Roux, S. T. Rakotonarivo, C. Marandet, W. A. Kuperman, "Target localization through a data-based sensitivity kernel: A perturbation approach applied to a multistatic configuration", The Journal of Acoustical Society of America, 135, 1800-1807 (2014), DOI:http://dx.doi.org/10.1121/1.4868362

Chapter 4

Active probing using ambient noise, without active sources

We here investigate whether a correlation based processing of acoustical noise can be used as a surrogate for acoustic sensing with the active sources in a reverberating medium, which is the same cylindrical tank used in Chapter three. In particular, we demonstrate that the transfer function from active sources to receivers can be obtained passively from the ambient noise recorded in the tank. The proposed approach is validated experimentally inside a fish tank of 5.6m-diameter and water depth of 1.05m; acoustic sources and receivers are located on the periphery of the tank.

4.1 Introduction

Early work has shown that random noise data contains information about the environment, and this information can be extracted when the noise recordings are processed appropriately.

Although random noise sources are typically considered incoherent, coherent processing of noise recordings is possible, as there is some spatial coherence between sensors that receive sound from the same individual noise source. If you imagine two receivers both embedded in a random noise field, the impulse response between two receivers can be estimated by cross-correlating long-duration ambient noise from them [45, 46]. The arrival times and strengths of the cross correlation peaks emerge from the accumulated contributions from noise sources whose propagation path pass through both receivers. This approach has been expanded to ultrasonics [45, 47, 48], underwater acoustics [49, 50, 51], structural-health monitoring [52, 53], and geoacoustic imaging [54, 55, 56]. In addition, using surface velocity and intensity fields, a similar method in helioseismology is developed to image the propagation of solar waves through sunspots [57, 58, 59, 60].

This study focuses on using coherent processing of ambient noise recordings resident in a fish tank for extracting the local transfer function between the sensors. The data results show that the ambient noise is dominant in the frequency band $f < 4$ kHz, and we have analyzed data in frequency bands of $f = 0.5 - 1.5$ kHz, $f = 1 - 3$ kHz, $f = 2 - 4$ kHz to compare with the active measurements. By comparing the active

and passive measurements, we show that it is possible to extract the local time domain Green's function from ambient noise as recorded on 16 spatially separated receivers located on the periphery of the tank.

This Chapter includes four sections. Following this Introduction, Section II introduces theory. Section III experimental set-up, initial data analysis where active and passive measurements are compared. The last section summarizes the findings from this study.

4.2 Theory

Here, we show a formulation of the ambient noise cross-correlation function.

Based on theoretical and experimental results, [75, 76, 49] it has been shown that the time derivative of the noise cross correlation function (NCF) approximately gives the sum of the TDGF as [76]

$$\frac{d_{a,b}(\tau)\rangle}{d\tau} \approx -G(\vec{r}_a,\vec{r}_b;\tau) + G(\vec{r}_b,\vec{r}_a;-\tau) \tag{4.1}$$

where $C_{a,b}(\tau)$ represents the cross-correlation of the signals between two receivers a and b located at $\vec{r}_a$ and $\vec{r}_b$, respectively, and τ is the time delay between the receivers (see geometry in Figure 4.1) In a stationary medium the NCF, $C_{a,b}(\tau)$, is given by

$$C_{a,b}(\tau) = \int_{-T/2}^{T/2} p(r_a;t)p(r_b;t+\tau)dt \tag{4.2}$$

where p is the pressure field recorded at each sensor, and T is the time over which the correlation is being performed. Given an ambient noise field propagating through the sensors, the resulting time series can approximate the time-of-arrival structure of the Green's function between the two sensors as if one of them was a source and the other a receiver [49, 77, 76, 75, 78, 79]. Here, TDGF which comes from noise events propagate from receiver a to b and yields a positive correlation time-delay τ and the time−reversed TDGF which comes from noise events propagate from receiver b to a and yields a negative correlation time-delay -τ. Therefore, in case of uniformly distributed noise sources, the NCF between the two sensors will be a symmetric function with respect to the arrival time. (In this study, an average of the correlations for the positive and negative time-delays is taken to be used as "new" positive correlations, and then it is symmetrized to be used as negative time-delays.

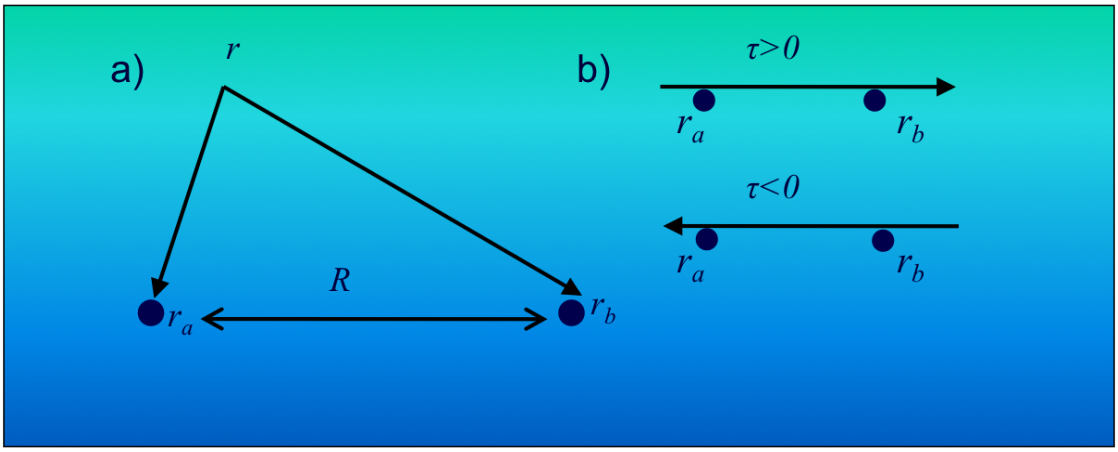

Figure 4.1: a) Schematic of the geometric variables for the waves traveling from location r to the two receivers at r_a and r_b, that are separated by a distance R. b) The waves propagation towards the right correlate for a positive time delay $\tau > 0$, whereas the waves traveling towards the left correlate for a negative time delay $\tau < 0$

In practice, the NCF is constructed from ensemble averages over realizations of the noise source signals and the signals recorded by receivers a and b are correlated only over a finite interval T including both positive and negative time delays. A measure of the variance $Var(C_{a,b}(\tau))$ gives an estimate of the residual error done when approximating the TDGF by the time derivative of the NCF. Therefore, it is a key quantity to evaluate. To estimate the emergence rate of the convergence time, we define a signal-to-noise ratio (SNR). The SNR of the noise correlation function in this study is defined as the ratio (in dB) of the peak amplitude in a time window of interest centered around the main arrivals and the square root of the variance of the time derivative of noise correlation function in a time window, which includes incoherent signal (e.g., see Figure 4.4), [80].

4.3 Experiment results

4.3.1 Experiment set-up

Figure 4.2.(a) shows the experimental setup that includes a fish tank of 5.6 m-diameter and water depth of 1.05 m. The receiver transducers are located on a sensor cable of which diameter is 5.2m, and the depth of the sensors vary between 0.2 m and 0.8 m. There are eight sources, spaced by approximately 2 m, and 16 receivers, spaced by approximately 1 m.

For active measurements, signal acquisition starts with transmission of a two period pulse centered at $f = 10$ kHz. The pulse is generated at source s_1 and the tank's

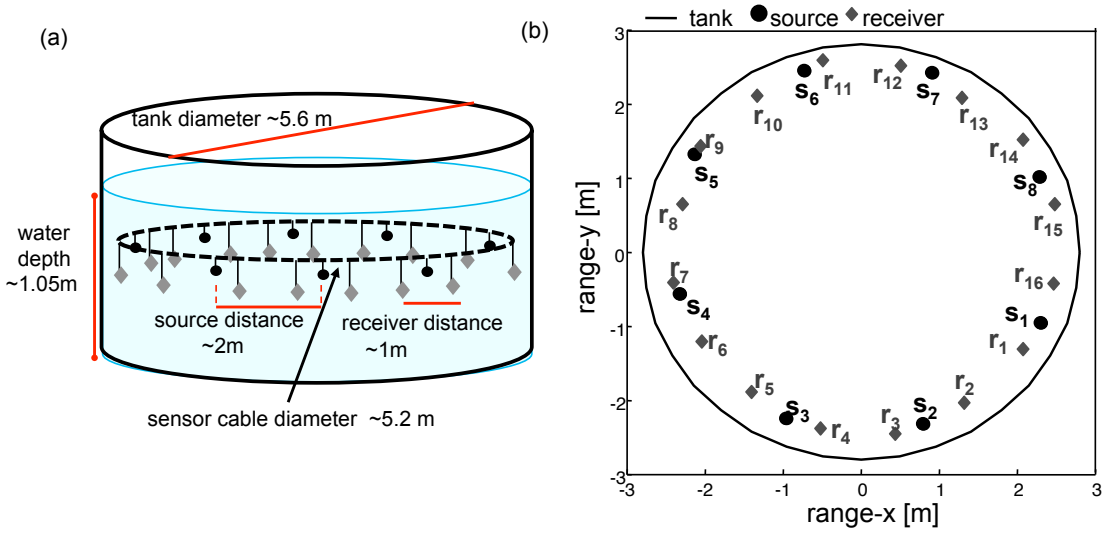

Figure 4.2: (a) Experimental set-up, with a tank of 5.6 m in diameter and a water depth of 1.05 m. The set-up includes eight sources with $\sim$ 2 m inter-element spacing and 16 receivers with $\sim$ 1 m inter-element spacing. The depth of the sensors vary between 0.2 m, and 0.8 m. b) The source$-$receiver geometry. For passive case, all sources are turned off, and 16 receivers record ambient noise resident in the tank.

acoustic response is recorded on all of the 16 receivers (see Fig. 4.2(b) for the geometry of the system). Having completed the acquisition between source s_1 and receivers r_{1-16}, the same pulse is transmitted from all of the other sources in a sequential manner. One round of signal acquisition, with transmission between eight sources and 16 receivers, takes t=5 s, which is referred to here as one *shot*. After a set of four *shots* is completed (20 s), the data is saved as 20-sec files. For ambient noise recordings, data is collected at 16 receivers and is saved as 20-sec files for a continuous recording of $\sim$6 hours.

4.3.2 Overview of data

The frequency spectrum from one receiver r_1 over the 200-minute target-free experiment is shown in Figure 4.3. Prior to computing the cross$-$correlation functions,

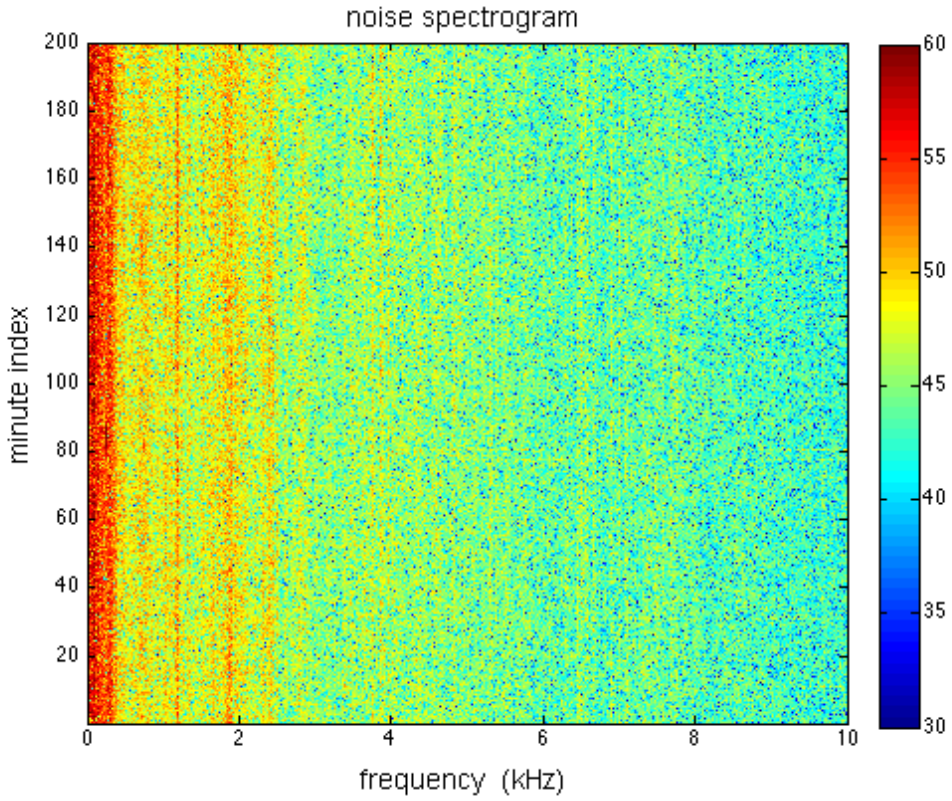

Figure 4.3: Spectrogram of ambient noise data recorded over 200-minute. Horizontal axis show the frequency range up to 10kHz. Vertical axis gives the minute index. Colorbar is in dB.

each 20-sec long ambient noise recording was filtered for the frequency band from $f = 0.5 - 1.5$ kHz, $f = 1 - 3$ kHz, and $f = 2 - 4$ kHz. The decision to use those bands was made based on the noise spectrograms, as main part of the energy is below 5kHz, and also to compare to the active measurements. The data were further homogenized by (1) frequency-whitening the amplitude spectrum of the data to diminish strong spectral peaks and by (2) clipping the signal amplitudes that are above a threshold, as these two pre-processing steps reduce the high amplitude noise events' influence while preserving the phase information and the arrival-time structure of the noise correlations. The pre-

processing steps mentioned here have been described in further detail in previous studies [76, 81].

We can start off our analysis by looking at the correlations between an individual sensor pair. A sample of $t = 20$ second correlation between the receivers r_1 and r_8 is shown in Figure 4.4. To investigate the rate at which TDGF emerges as a function of averaging time, the SNR is defined as the ratio (in dB) of the peak amplitude in a $t = 100$ ms time window centered around the main arrivals and the standard deviation of a time window $t = 500 - 600$ ms of the time derivative of noise correlation function [80]. The arrival time structure of the correlation of ambient noise corresponds to the propagation of coherent noise signals between receivers. Although the signals are buried within the incoherent noise, through averaging, the coherent signals will build up, and provide with the arrival-time structure of the time domain Green's function, which is what we need to extract from the ambient noise recordings.

Figure 4.5 shows the SNR with increasing time averaged in the NCF, for the given sensor pair ($r_1 - r_8$). The horizontal axis shows the averaging time (in log10) and vertical axis shows the SNR (in log10). Here each green line corresponds to a 50-minute averaging of 20-sec accumulations, with 50 percent overlaps. The red line corresponds to the average of the 50-minute averaged correlations. It is clear that the increase in SNR is proportional to the square root of recording time, in agreement with [75, 82],

$$\frac{log_{10}SNR}{log_{10}t} \approx 0.5 \tag{4.3}$$

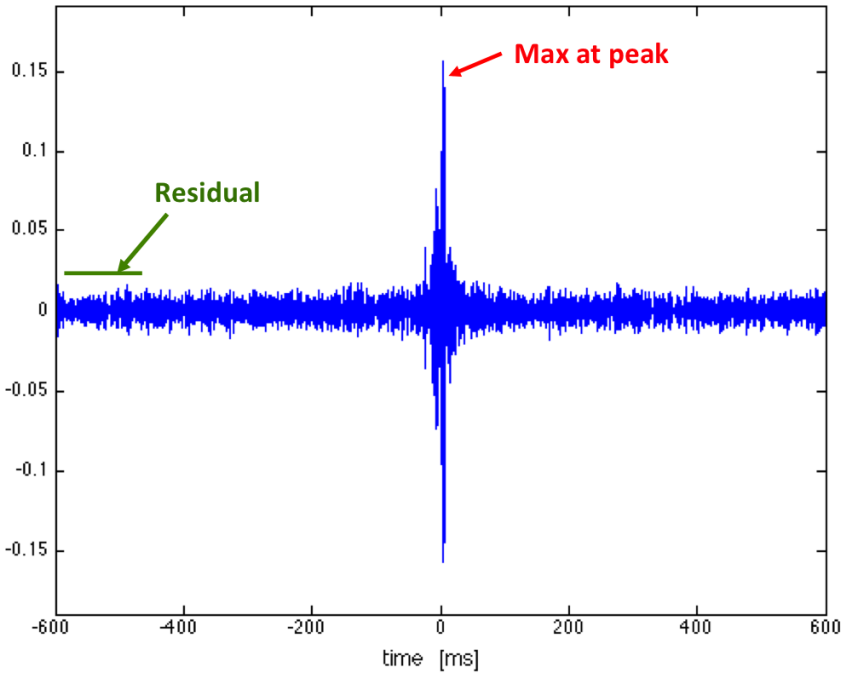

Figure 4.4: A sample of 20-sec noise correlations for the reference field between r_1 and receiver r_8. The SNR is the ratio (in dB) of the peak amplitude in a t=100 ms time window centered around the main arrivals and the standard deviation of a time window t=500-600 ms

Based on the results in Figure 4.5, an averaging time of 20-minute is taken as the emergence rate of NCF, as this emergence rate of 20-min is confirmed with the other receivers.

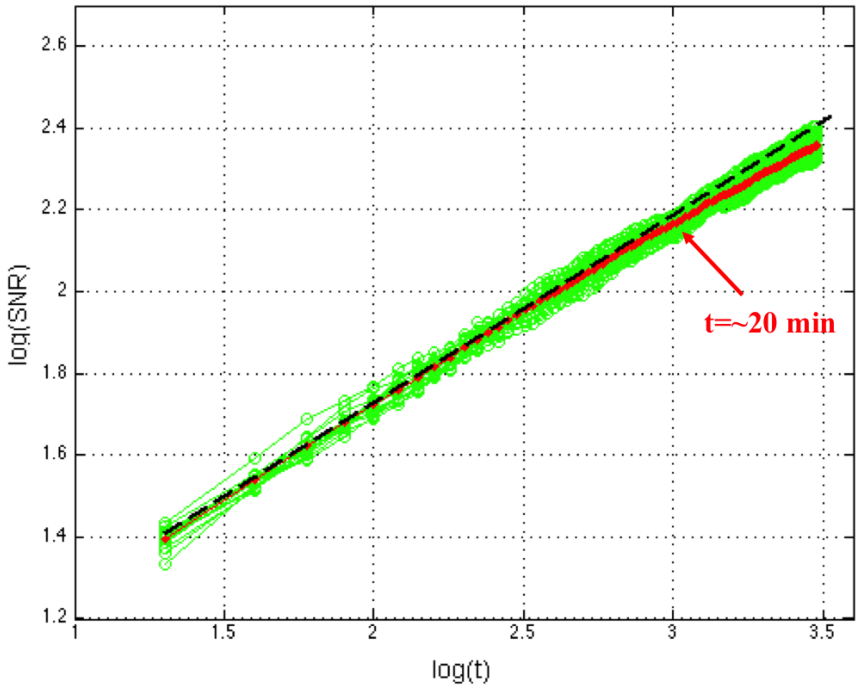

Figure 4.5: SNR build up for the given sensor pair ($r_1 - r_8$). The horizontal axis shows the averaging time (in log10) and vertical axis shows the SNR (in log10). Each green line represents a 50-minute averaging of 20 second accumulations, with 50 percent overlaps; and red line corresponds to the average of the 50-minute averaged correlations. Black dashed line corresponds to the theoretical line, 0.5.

4.3.3 Active vs. Passive

Figure 4.6 shows time series of active measurements in the frequency band of $f = 6 - 14$ kHz. An average of 1-min active data is used for results shown here. As we aim to compare passive and active data, here we symmetrize the time series around $t = 0$ sec. The time series represent the acoustic response of the fish tank with two different location of source sensor relative to the 16 receivers: from source s_1 to all of the 16 receivers (Figure 4.6).(a)), and from source s_5 to all of the 16 receivers (Figure 4.6). (b)). The experimental arrival times are favorably matching expected arrival times, represented by red dots.

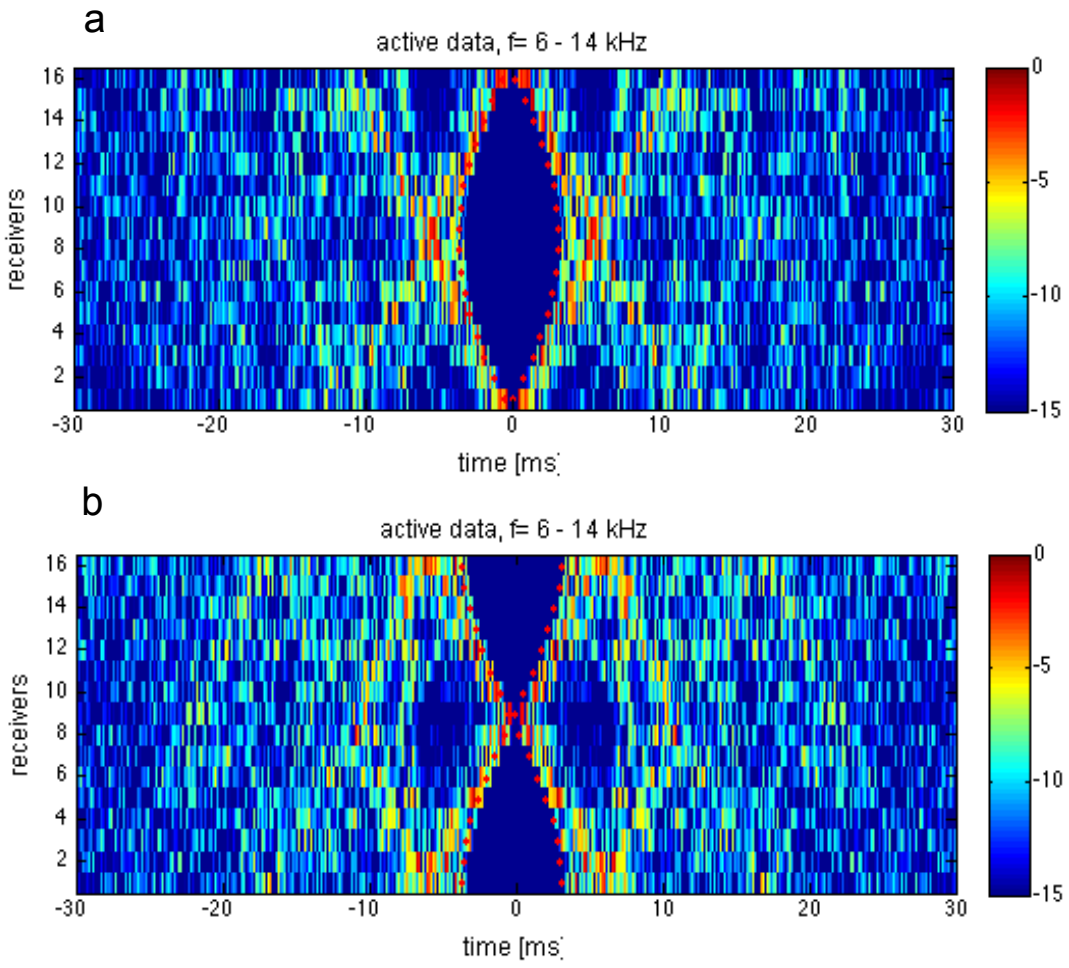

Figure 4.6: Measurements from active sources at $f = 6 - 14$ kHz (a) source s_1, (b) source s_5 to all of the 16 receivers yield the acoustic response (transfer function) of the tank

As the motivation of this study is to emulate active sources using ambient noise, we then analyze active data in a low frequency regime where the passive noise energy is concentrated. The source characteristic curve in Figure 4.7 shows that, it is possible to analyze active data at around f=1 Hz, although it will be ~ 40 dB down from the operating frequency band of the source transducer.

Figure 4.8 , 4.9 , 4.10 , shows comparisons of active time series and noise cor-

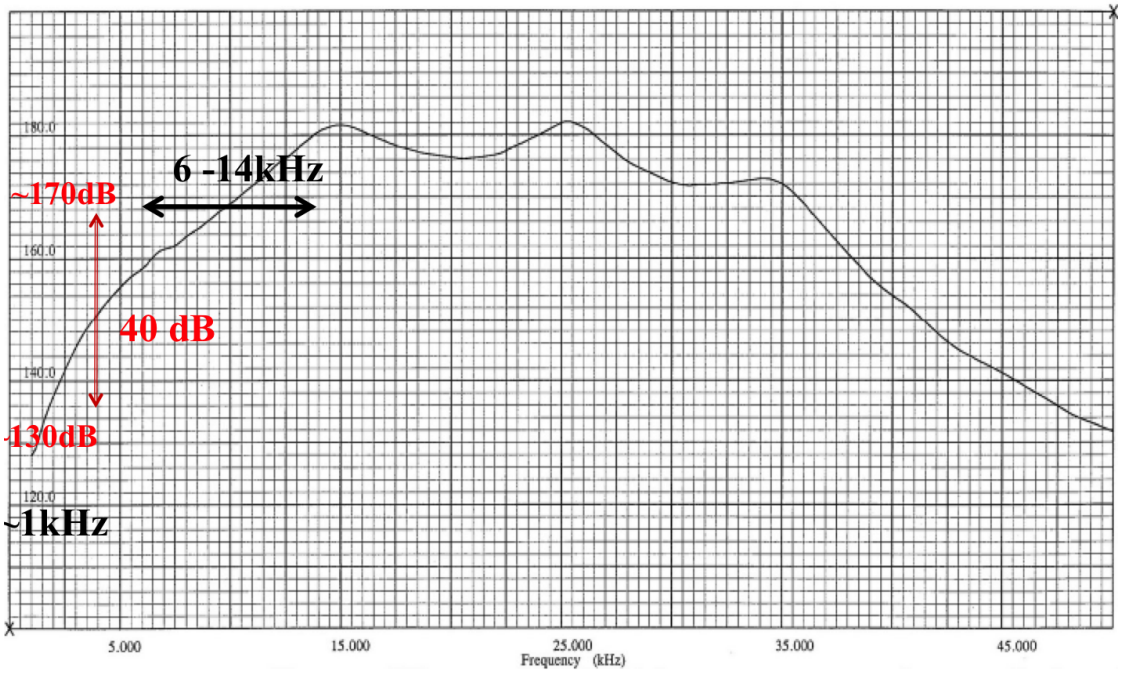

Figure 9. Sound Pressure Level (dB re µPa @ 1m) versus frequency for PWM amplifier driving ITC-1001 (6 dB down from full power)

Figure 4.7: Characteristic curve of the sources used. Moving from $f = 6 - 14$ kHz down to $f =$ 1 kHz means 40 dB down.

relations, normalized to their maximum, filtered at $f = 0.5 - 1.5$ kHz, $f = 1 - 3$ kHz, and $f = 2 - 4$ kHz, respectively. For passive data results, an average of 20-min cross-correlations are used, based on the emergence rate of NCF (see Figure 4.5). To compare the arrival time structure of ambient noise to the active sources, we have used reference receivers adjacent to the refrence sources. For instance, for the time series from source s_1 to all of the 16 receivers will have a similar structure with correlations of reference receiver of r_1 and all of the 16 receivers, as receiver r_1 and source s_1 are adjacent and the spacing between them is 0.4m. To compare active time series from source s_5 to receivers, we have correlated receiver r_9 with all of the 16 receivers, as spacing between source s_5 and receiver r_9 is 0.13m (for source-receiver geometry see Figure 4.2).

The x-axis shows time in second for active data, and correlation time in second for ambient noise data. The y-axis represents the 16 receivers (1) receiving signals from a specific source in active case, or (2) correlated with the reference receiver. Four different subplots in each figure represents (a) active data from source s_1 to the 16 receivers, (b) active data from source s_5 to the 16 receivers, (c) noise correlations of 16 receivers with the receiver r_1, (d) noise correlations of 16 receivers with the receiver r_9.

In lower frequency band, the transfer function of the tank calculated using noise correlations is in agreement with active measurements. In both cases, correlating receiver r_1 and r_9 and all of the receivers, the time of the arrivals are extracted accurately for the direct path, and also for second reflections from tank walls (see second reflections in active case Figure 4.6). With increasing frequency band, the SNR of active data gets stronger whereas the SNR of noise-correlations starts to get weaker, which is consistent with the frequency spectrum of the noise we shown in Figure 4.3.

Generally when we determine the arrival time of a signal we are interested in the direct path between the sensors, or from a modeled source to a receiver. A further study would be to improve the arrival structures to get a better estimation of the time of the arrivals which would be use for a possible target detection or localization application. Depending on the practical applications, one can decide which frequency band to use. For instance, it is not possible to locate the target with a size less than 10 cm, as in Chapter three. To be able to work in the lower frequency, perhaps a target of length/size of $\sim$ 1m need be considered.

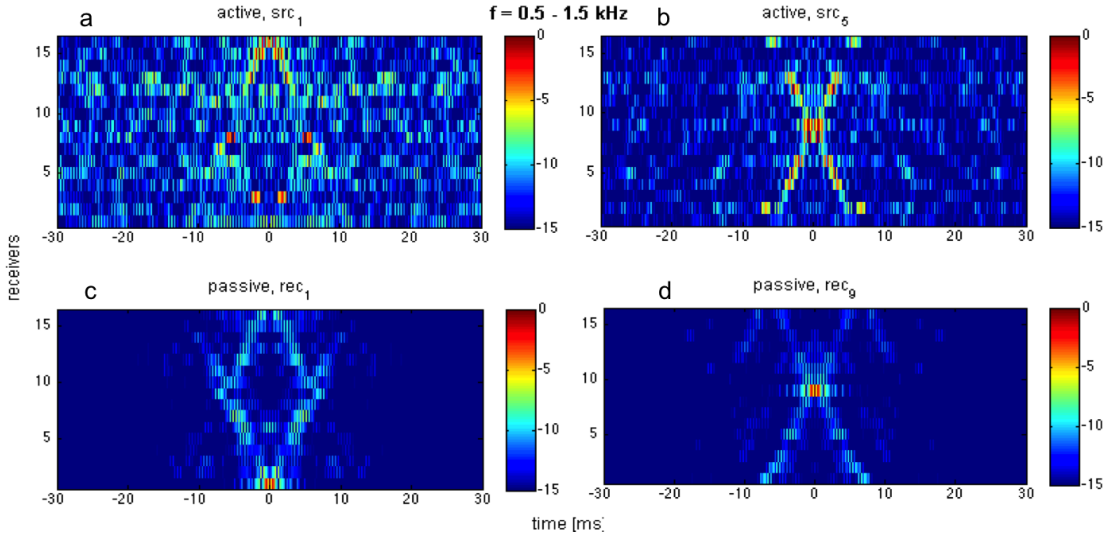

Figure 4.8: Acoustic response of fish tank at $f = 0.5 - 1.5$ kHz (a) active with source s_1, (b) active with source s_5, (c) passive with receiver r_1, (d) passive with receiver r_9

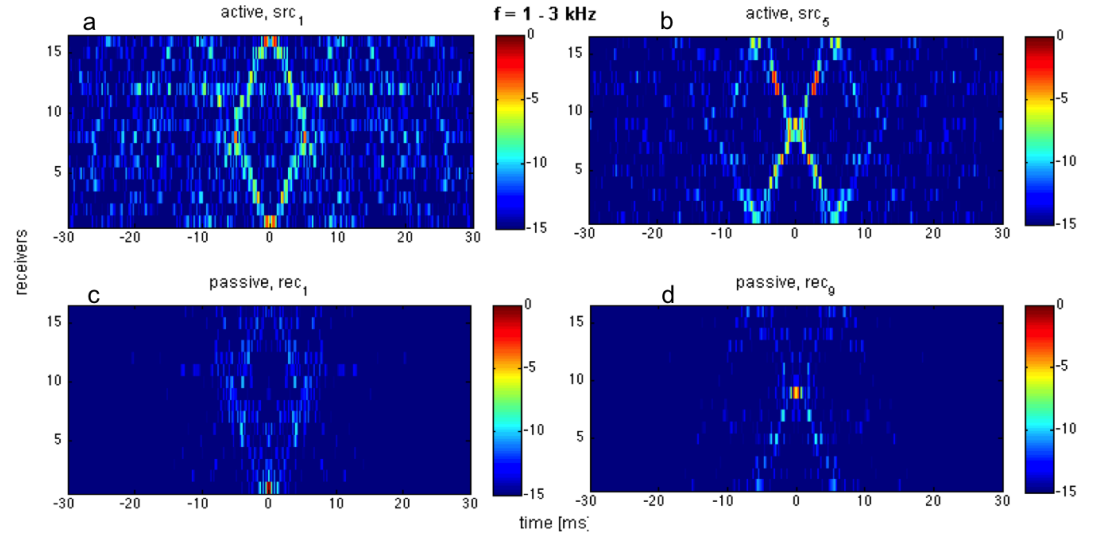

Figure 4.9: Acoustic response of fish tank at $f = 1 - 3$ kHz (a) active with source s_1, (b) active with source s_5, (c) passive with receiver r_1, (d) passive with receiver r_9

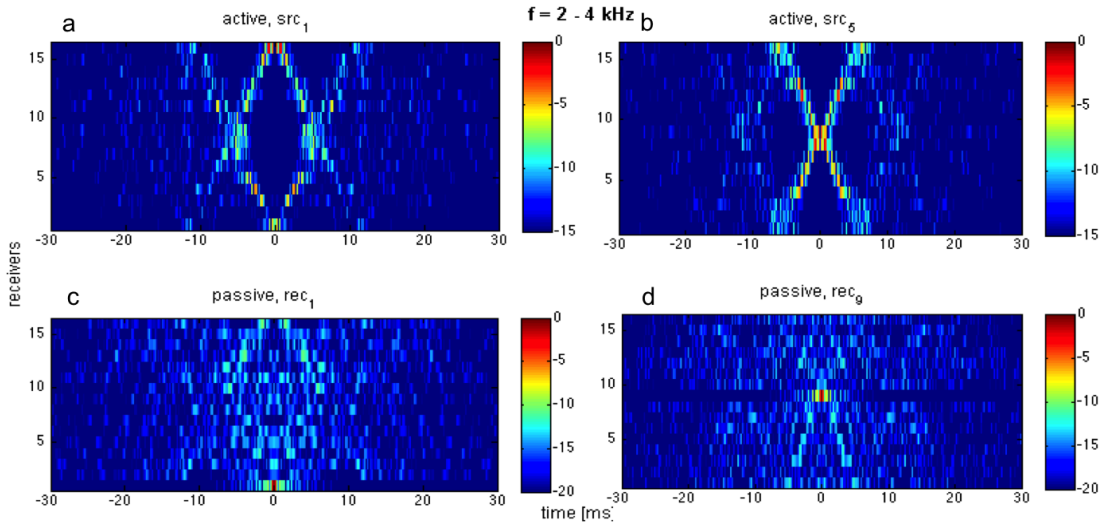

Figure 4.10: Acoustic response of fish tank at $f = 2-4$ kHz (a) active with source s_1, (b) active with source s_5, (c) passive with receiver r_1, (d) passive with receiver r_9

4.4 Conclusion

The experimental data obtained in a reverberating tank were analyzed using coherent processing of ambient noise recordings, and compared to the results obtained using active sources. The differencing approach is implemented in terms of cross-correlations, and the analysis is done over several frequency bands for $f = 0.5-1.5$ kHz, $f = 1-3$ kHz, and $f = 2-4$ kHz. Furthermore, it was shown that the amplitude of the coherent waveforms build up proportionally to the square root of the recording time. Using only the ambient noise recorded at the receivers, the local time domain Green's function was accurately extracted. The study is a validation of active probing without active sources in a laboratory experiment.

4.5 Acknowledgments

This project is funded by the Office of Naval Research (ONR).

Chapter 5

Conclusions

This thesis presented data-based acoustic and seismoacoustic sensing methods using minimum a priori information with a focus on differencing approaches. The main conclusion from Chapter two, three, and four, respectively, is that it is possible to (1) extract seismic information without using seismometers, (2) perform an active localization without a complex propagation model, and (3) perform an active probing using only ambient noise. The differencing approaches in each Chapter are implemented as (1) acoustic pressure field differences for estimation of the vector quantities analogous to seismic data, (2) change in field amplitudes between target-free and target-present cases, (3) cross-correlations as a measure of the difference of ambient noise recorded at the receivers.

In chapter two, we show that it is possible to extract low-frequency seismic information without using seismometers. We have used IMS hydroacoustic network data in the very low frequency regime ($f = 0.01 - 0.05$ Hz), to demonstrate that these sta-

tions can also be used as water column seismometers. The differencing approach is implemented as the gradient of the pressure fields. Measuring the pressure gradient between two closely separated (with respect to wavelength) points is equivalent to a velocity measurement. Thus within this low frequency band, by differencing the acoustic pressure, we obtain vector quantities analogous to what a seismometer would record. Comparing processed hydrophone station records of the 2004 Great Sumatra-Andaman Earthquake with broadband seismograms from a nearby island station, we find that the differenced hydrophones are indeed a practical surrogate for seismometers. Consistent with the physics, transverse Love waves in the water column do not couple, whereas P waves and Rayleigh waves with radial and vertical motion do couple. A slowness analysis using only the pressure recordings at the three hydrophones has shown that it is possible to determine the direction of the source location at a single IMS hydrophone station.

In chapter three, experimental data from a highly reverberating tank were analyzed for target localization using a data-based sensitivity kernel approach. The experiment consisted of measurements without the target, and with the target at a sparse set of points inside the tank. The differencing approach is implemented as the change in the amplitude between target-free and target-present fields. Experimental sensitivity kernel is constructed for the target at the grid points using the direct path arrivals, and compared to the theoretical sensitivity kernel. Having shown that experimental sensitivity kernel matches the theoretical sensitivity kernel, a target localization is implemented (1) using only the direct-path, and (2) including later arrivals. The experimental observa-

tions show that target localization is successful using only the direct path, and including later arrivals from the tank wall and the bottom/surface reverberation enhances the localization results.

Finally, chapter four examined ambient noise measured inside a cylindrical tank. The amplitude of the coherent waveforms build up proportionally to the square root of the recording time. By comparing with active sources, we have shown that it is possible to estimate the tank's acoustic response (i.e. Green's function) using only ambient noise. The arrival structure of the noise correlations were found to match with the expected arrival times. Hence, the work presented here is a validation of active probing without active sources in a laboratory set-up.

Bibliography

[1] E. Okal, "T-phase stations for the international monitoring system of the Comprehensive Nuclear-Test Ban Treaty: a global perspective", Seism Res Lett **72**, 186–196 (2001).

[2] M. Lawrence and P. Grenard, "Hydroacoustic monitoring system for the Comprehensive Nuclear-Test-Ban Treaty", OCEANS '98 Conference Proceedings **2**, 694–697 (1998).

[3] de Groot-Hedlin Catherine D., "Estimation of the rupture length and velocity of the Great Sumatra earthquake of dec 26, 2004 using hydroacoustic signals", Geophys. Res. Lett. **32**, L11303 (2005).

[4] M. Tolstoy and D. Bohnenstiehl., "Hydroacoustic contributions to understanding the december 26th 2004 Great Sumatra-Andaman earthquake", Surveys in Geophysics **27**, 633–646 (2005).

[5] M. Tolstoy and D. Bohnenstiehl., "Analysis of hydroacoustic signals in the Indian Ocean", 24th Seismic ResearchReview, Nuclear Explosion Monitoring: Innovation and Integratione, (2002).

[6] E. Chapp, D. Bohnenstiehl, and M. Tolstoy., "Sound-channel observations of ice-generated tremor in the Indian Ocean", Geochem. Geophys. Geosyst. **6**, Q06003 (2005).

[7] B. Li and A. Gavrilov, "Localization of antarctic ice breaking events by frequency dispersion of the signals received at a single hydroacoustic station in the Indian Ocean", The Journal of the Acoustical Society of America **123**, 2990–2990 (2008).

[8] F. Graeber and P. Piserchia, "Hydroacoustic contributions to understanding the december 26th 2004 zones of t-wave excitation in the ne Indian Ocean mapped using variations in backazimuth over time obtained from multi-channel correlation of ims hydrophone triplet data", Geophys J. Int. **158**, 239–256 (2004).

[9] J. Hanson and H. Givens, “Accurate azimuthal estimates from large aperture hydrophone array using t-phase waveforms”, Geophys. Res. Lett. **25**, 365–368 (1998).

[10] E. D. Pezzo and F. Giudicepietro, “Plane wave fitting method for a plane, small aperture, short period seismic array: a mathcad program. using t-phase waveforms.”, Computational Geoscience **28**, 59–64 (2002).

[11] Y. Cansi, “An automatic seismic event processing for detection and location: The p.m.c.c. method”, Geophys. Res. Lett. **22**, 1021–1024 (1995).

[12] C. Fox, H. Matsumoto, and T. Lau, “Monitoring Pacific Ocean seismicity from an autonomous hydrophone array”, J Geophys Res **106**, 4183–4206 (2001).

[13] A. Nehorai and E. Paldi, “Acoustic vector-sensor array processing”, IEEE Trans. Signal Processing **42**, 2481–2491 (1994).

[14] B. Hochwald and A. Nehorai, “Identifiability in array processing models with vector-sensor applications”, IEEE Trans. Signal Processing **44**, 83–95 (1996).

[15] M. Hawkes and A. Nehorai, *"Bearing estimation with acoustic vector-sensor arrays," in Acoustic Particle Velocity Sensors: Design, Performance, and Applications* ((M. J. Berliner and J. F. Lindberg,) (1996).

[16] M. Hawkes and A. Nehorai, “Acoustic vector-sensor beamforming and capon direction estimation”, IEEE Trans. on Signal Processing **46**, 2291–2304 (1998).

[17] G. W. Wolf, “U.s. navy sonobuoys key to antisubmarine warfare”, Sea Technol. **39**, 41–44 (1998).

[18] O. Wilson, S. Wolf, and F. Ingenito, “Measurements of acoustic ambient noise in shallow water due to breaking surf”, J. Acoust. Soc. Am. **78**, 190–195 (1985).

[19] A. M. Thode, G. L. D’Spain, and W. A. Kuperman, “Matched-field processing, geoacoustic inversion, and source signature recovery of blue whale vocalizations”, J. Acoust. Soc. Am. **107**, 1286–1300 (2000).

[20] M. McDonald, “DIFAR hydrophone usage in whale research”, Can. Acoust. **32**, 155–160 (2004).

[21] C. Greene, M. McLennan, R. Norman, T. McDonald, R. Jakubczak, and W. Richardson, “Directional frequency and recording (DIFAR) sensors in seafloor recorders to locate calling bowhead whales during their fall migration”, J. Acoust. Soc. Am. **116**, 799–813 (2004).

[22] G. L. D’Spain, J. Luby, G. Wilson, and R. Gramann, “Vector sensors and vector sensor line arrays: Comments on optimal array gain and detection”, J. Acoust. Soc. Am. **120**, 171–185 (2006).

[23] K. Smith and A. van Leijen, "Steering vector sensor array elements with linear cardioids and nonlinear hippioids", J. Acoust. Soc. Am. **122**, 370–377 (2007).

[24] G. L. D'Spain, W. S. Hodgkiss, and G. L. Edmonds, "Energetics of the deep ocean's infrasonic sound field", The Journal of the Acoustical Society of America, **89**, 1134–1158 (1991).

[25] S. Coraluppi and D. Grimmett, "Multistatic sonar tracking", Proceedings of the SPIE Conference on Signal Processing, Sensor Fusion, and Target Recognition XII **5096**, 399–410 (2003).

[26] S. Coraluppi, "Multistatic sonar localization", Oceanic Engineering, IEEE Journal of **31**, 964–974 (2006).

[27] I. Bekkerman and J. Tabrikian, "Target detection and localization using mimo radars and sonars", Signal Processing, IEEE Transactions on **54**, 3873–3883 (2006).

[28] S. Kim, B. Ku, W. Hong, and H. Ko, "Performance comparison of target localization for active sonar systems", Aerospace and Electronic Systems, IEEE Transactions on **44**, 1371–1380 (2008).

[29] J. Edwards, H. Schmidt, and K. LePage, "Bistatic synthetic aperture target detection and imaging with an AUV", Oceanic Engineering, IEEE Journal of **26**, 690–699 (2001).

[30] W. Kuperman, T. Akal, W. Hodgkiss, S. Kim, G. Edelmann, and H. Song, "Forward-scatter barrier with a time-reversal mirror", The Journal of the Acoustical Society of America **108**, 2607–2607 (2000).

[31] K. G. Sabra, S. Conti, P. Roux, T. Akal, W. A. Kuperman, J. M. Stevenson, A. Tesei, and P. Guerrini, "Experimental demonstration of a high-frequency forward scattering acoustic barrier in a dynamic coastal environment", The Journal of the Acoustical Society of America **127**, 3430–3439 (2010).

[32] H. Song, W. Kuperman, W. Hodgkiss, T. Akal, and P. Guerrini, "Demonstration of a high-frequency acoustic barrier with a time-reversal mirror", Oceanic Engineering, IEEE Journal of **28**, 246–249 (2003).

[33] M. Stevenson, A. Tesei, P. Guerrini, T. Folegot, K. Sabra, H. Roux, P.and Song, W. Kuperman, W. Hodgkiss, and T. Akal, "An acoustic tripwire based on forward scattering in a time-reversal mirror", US Navy J. Underwater Acoust **61**, 52–60 (2007).

[34] K. G. Sabra, P. Roux, H.-C. Song, W. S. Hodgkiss, W. Kuperman, T. Akal, and J. M. Stevenson, "Experimental demonstration of iterative time-reversed reverberation focusing in a rough waveguide. application to target detection", The Journal of the Acoustical Society of America **120**, 1305–1314 (2006).

[35] T. Folegot, G. Martinelli, P. Guerrini, and J. Stevenson, "An active acoustic tripwire for simultaneous detection and localization of multiple underwater intruders", The Journal of the Acoustical Society of America **124**, 2852–2860 (2008).

[36] C. Marandet, P. Roux, B. Nicolas, and J. Mars, "Target detection and localization in shallow water: An experimental demonstration of the acoustic barrier problem at the laboratory scale", The Journal of the Acoustical Society of America **129**, 85–97 (2011).

[37] J. Sarkar, B. D. Cornuelle, and W. A. Kuperman, "Information and linearity of time-domain complex demodulated amplitude and phase data in shallow water", The Journal of the Acoustical Society of America **130**, 1242–1252 (2011).

[38] E. Skarsoulis and B. Cornuelle, "Travel-time sensitivity kernels in ocean acoustic tomography", The Journal of the Acoustical Society of America **116**, 227–238 (2004).

[39] P. Roux, I. Iturbe, B. Nicolas, J. Virieux, and J. I. Mars, "Travel-time tomography in shallow water: Experimental demonstration at an ultrasonic scale", The Journal of the Acoustical Society of America **130**, 1232–1241 (2011).

[40] J. Sarkar, C. Marandet, P. Roux, S. Walker, B. D. Cornuelle, and W. A. Kuperman, "Sensitivity kernel for surface scattering in a waveguide", The Journal of the Acoustical Society of America **131**, 111–118 (2012).

[41] M. Woodward, "Wave−equation tomography", Geophysics **57**, 15–26 (1992).

[42] F. Dahlen and A. Baig, "Frechet kernels for body-wave amplitudes", Geophysical Journal International **150**, 440–466 (2002).

[43] P. Roux, C. Marandet, B. Nicolas, and W. A. Kuperman, "Experimental measurement of the acoustic sensitivity kernel", The Journal of the Acoustical Society of America **134**, EL38–EL44 (2013).

[44] M. J. Buckingham, B. V. Berkhout, and S. A. L. Glegg, "Imaging the ocean with ambient noise", Nature **356** (1992).

[45] R. Weaver and O. Lobkis, "On the emergence of the Green's function in the correlations of a diffuse field", J. Acoust. Soc. Am. **110**, 3011–3017 (2001).

[46] R. Weaver and O. Lobkis, "Ultrasonics without a source: Thermal fluctuation correlations at mhz frequencies,", Phys. Rev. Lett. **87**, 134301 (2001).

[47] E. Larose, A. D. A, M. Campillo, and M. Fink, "Imaging from one-bit correlations of wideband diffuse wave fields", Journal of Applied Physics 8393–8399 (2004).

[48] S. Lani, S. Satir, G. Gurun, K. Sabra, and F. L. Degertekin., "High frequency ultrasonic imaging using thermal mechanical noise recorded on capacitive micromachined transducer arrays.", Applied Physics Letters 224103 (2011).

[49] P. Roux, W. A. Kuperman, and the NPAL Group, "Extracting coherent wave fronts from acoustic ambient noise in the ocean", J. Acoust. Soc. Am. **116**, 1995–2003 (2004).

[50] K. G. Sabra, P. Roux, A. M. Thode, G. L. D'Spain, W. Hodgkiss, and W. Kuperman, "Using ocean ambient noise for array self-localization and self-synchronization", IEEE J. Ocean. Eng. **30**, 338–347 (2005).

[51] M. Siderius, C. H. Harrison, and M. B. Porter, "A passive fathometer technique for imaging seabed layering using ambient noise", J. Acoust. Soc. Am. **120**, 1315–1323 (2006).

[52] E. Larose, P. Roux, and M. Campillo., "Reconstruction of Rayleigh-lamb dispersion spectrum based on noise obtained from an air-jet forcing", J. Acoust. Soc **122**, 3437–3444 (2007).

[53] K. Sabra, E. Winkel, B. D.A., B. Elbing, S. Ceccio, M. Perlin, and D. Dowling., "Using cross correlations of turbulent flow-induced ambient vibrations to estimate the structural impulse response:application to structural health monitoring", J. Acoust. Soc. Am. 1987–1995 (2007).

[54] K. G. Sabra, P. Gerstoft, P. Roux, W. A. Kuperman, and M. C. Fehler, "Surface wave tomography from microseism in Southern California", Geophs. Res. Lett. **32** (2005b).

[55] N. Shapiro and M. Campillo, "Emergence of broadband Rayleigh waves from correlations of the ambient seismic noise", Geophys. Res. Lett **31**, L07614 (2004).

[56] N. Shapiro, L. S. M. Campillo, and M. H. Ritzwoller, "High resolution surface wave tomography from ambient seismic noise", Science **307**, 1615–1618 (2005).

[57] T. L. Duvall Jr, S. Jefferies, J. W. Harvey, and M. A. Pomerantz, "Time-distance helioseismology", Narture **362**, 430–432 (1993).

[58] L. Gizon and A. C. Birch, "Time-distance helioseismology: The forward problem for random distributed sources", Astrophys. J. **571**, 966–986 (2002).

[59] L. Gizon and A. C. Birch, "Local helioseismology", Living Rev. Solar Phys. **2** (2005), online Article: cited 15 November 2005.

[60] L. Gizon, "Tomography of the solar interior", Mod. Phys. Let. A **21**, 1701–1715 (2006).

[61] H. Matsumoto, J. Haxel, R. Dziak, D. Bohnenstiehl, and R. Embley, "Mapping the sound field of an erupting submarine volcano using an acoustic glider,", The Journal of the Acoustical Society of America **129**, EL94–EL99 (2011).

[62] M. Fehler, "Interaction of seismic waves with a viscous liquid layer", Bull. Seism. Soc. Am. **72**, 55–72 (1982).

[63] F. B. Jensen, W. A. Kuperman, M. B. Porter, and H. Schmidt, *Computational Ocean Acoustics*, AIP series in modern acoustics and signal processing (Springer-New York) (2011).

[64] J. Hanson and J. Bowman, "Dispersive and reflected tsunami signals from the 2004 Indian ocean tsunami observed on hydrophones and seismic stations", Geophys. Res. Lett. **32**, L17606 (2005).

[65] P. Goldstein, D. Dodge, M. Firpo, and L. Minne, *SAC2000: Signal processing and analysis tools for seismologists and engineers*, Invited contribution to The IASPEI International Handbook of Earthquake and Engineering Seismology (Academic Press, London,) (2003).

[66] H. P. Crotwell, T. Owens, and J. Ritsema, "The taup toolkit: Flexible seismic travel-time and ray-path utilities", Seismological Res. Lett. **70**, 154–160 (1999).

[67] J. Hanson, "Earthquake location applied to a mini-array: k-spectrum versus correlation method", 23rd Seismic Research Review, Jackson Hole, WY, Department of Energy,LA-UR-01-4454 **2**, 12–22 (2001).

[68] G. Masters, M. Barmine, and S. Kientz, *Mineos Version, 1.0.2 User Manual,CIG/CIT, Pasadena, California, USA,* (2011).

[69] A. Tesei and J. M. Stevenson, "A forward-looking acoustic barrier for detecting and tracking small underwater intruders- experimental results", Proc. Int. Conf. Underwater Ac. Measurements: Technologies and Results, Crete, Greece (2005).

[70] C. Prada, J. de Rosny, D. Clorennec, J.-G. Minonzio, A. Aubry, M. Fink, L. Berniere, P. Billand, S. Hibral, and T. Folegot, "Experimental detection and focusing in shallow water by decomposition of the time reversal operator", The Journal of the Acoustical Society of America **122**, 761–768 (2007).

[71] D. Clorennec, J. De Rosny, J.-G. Minonzio, C. Prada, M. Fink, T. Folegot, P. Billand, S. Tauvry, S. Hibral, and L. Berniere, "First tests of the dort method at 12 khz in a shallow water waveguide", in Proceedings IEEE Oceans Europe, Brest, France, **2**, 1205–1209 (2005).

[72] T. Folegot, P. Billand, S. Tauvry, S. Hibral, L. Berniere, J. De Rosny, D. Clorennec, J.-G. Minonzio, C. Prada, M. Fink, and B. Celestin, "Design of a time reversal

mirror for medium scale experiments", in Proceedings IEEE Oceans Europe, Brest, France **2**, 1210–1213 (2005).

[73] J. D. Rosny and P. Roux, "Multiple scattering in a reflecting cavity: Application to fish counting in a tank", The Journal of the Acoustical Society of America **109**, 2587–2597 (2001).

[74] S. Rakotonarivo, S. Walker, W. Kuperman, and P. Roux, "Localization of a small change in a multiple scattering environment without modeling of the actual medium", The Journal of the Acoustical Society of America **130**, 3566–3573 (2011).

[75] P. Roux, K. G. Sabra, and W. A. Kuperman, "Ambient noise cross correlation in free space: Theoretical approach", J. Acoust. Soc. Am. **117**, 79–94 (2005).

[76] K. G. Sabra, P. Roux, and W. A. Kuperman, "Emergence rate of the time-domain Green's function from the ambient noise cross-correlation function", J. Acoust. Soc. Am. **118**, 3524–3531 (2005).

[77] K. G. Sabra, P. Roux, and W. A. Kuperman, "Arrival-time structure of the time-averaged ambient noise cross-correlation function in an oceanic waveguide", J. Acoust. Soc. Am. **117**, 164–174 (2005).

[78] R. Snieder, K. Wapenaar, and U. Wegler, "Unified Green's function retrieval by cross-correlation; connection with energy principles", Phys. Rev. E. **75** (2007).

[79] R. Snieder, "Extracting the Green's function of attenuating heterogeneous acoustic media from uncorrelated waves", J. Acoust. Soc. Am. **121**, 2637–2643 (2007).

[80] K. G. Sabra, P. Gerstoft, P. Roux, W. A. Kuperman, and M. C. Fehler, "Extracting time-domain Green's function estimates from ambient seismic noise", Geophys. Res. Lett. **32** (2005a).

[81] A. Brooks and P. Gerstoft, "Green's function approximation from cross-correlations of 20-100 hz noise during a tropical storm", J. Acoust. Soc. Am. **125**, 723–734 (2009).

[82] R. Snieder, "Extracting the Green's function from the correlation of coda waves: A derivation based on stationary phase", Phys. Rev. E **69** (2004).